Intra-annual grounding-line migration and retreat: insights from high-resolution satellite and in-situ observations over Milne Glacier in the Canadian High Arctic

Yulia K. Antropova[1], Derek Mueller[1], Sergey V. Samsonov[2], Alexander S. Komarov[3], Jérémie Bonneau[4,5]

[1]Department of Geography and Environmental Studies, Carleton University, Ottawa, K1S 5B6, Canada
[2]Canadian Centre for Mapping and Earth Observations, Natural Resources Canada, Ottawa, K1A 0E4, Canada
[3]Data Assimilation and Satellite Meteorology Research Section, Environment and Climate Change Canada, Ottawa, K1A 0H3, Canada
[4]Department of Civil Engineering, The University of British Columbia, Vancouver, V6T 1Z2, Canada
[5]Département de Génie Civil et Génie des Eaux, Université Laval, Québec, G1V 0A6, Canada

Correspondence to: Yulia K. Antropova (YuliaAntropova@cmail.carleton.ca)

Abstract. Observing and quantifying ~~C~~changes ~~at~~ of the boundary where marine-~~-~~terminating glaciers transition from grounded to floating, known as the grounding line, ~~are~~ is critical for advancing our understanding of glacier stability~~. and ice discharge prediction. We explore changes in the ice flexure zone (FZ), which spans from the inland limit of tidal flexure, known as the hinge line, across the actual grounding line, to where the ice tongue becomes freely floating.~~ . The grounding line is difficult to observe directly but can be inferred from the ice surface tidal-flexure zone. This zone spans from the inland limit of tidal flexure — the hinge line, across the grounding line to the hydrostatic equilibrium line, where the ice tongue becomes freely floating. We explore ~~F~~flexure zone~~Z~~ ~~movements~~ changes on Milne Glacier, Nunavut, Canada from 2023 to 2024 ~~were measured~~ at a spatial resolution of 10 m using 4-day RADARSAT Constellation Mission (RCM) ~~repeat~~ data acquisitions from four different orbits. The ~~Double~~ Differen~~t~~ial~~e~~ Interferometric Synthetic Aperture Radar (~~D~~DInSAR) technique was employed to delineate 116 flexure zones through time~~FZ positions~~, which were then examined with respect to SAR viewing geometry, tides and atmospheric pressure, glacier velocity changes and ,ice bending, as well as ice surface and bed topography. The most reliable flexure zone delineation (horizontal uncertainty of ±8 m) was achieved with ascending RCM tracks at low incidence angles during periods when the ice velocity was steady and bending was not substantial, resulting in a combined SAR line-of-sight error of 0.13 cm. A worst-case flexure-zone delineation uncertainty of ±222 m was noted when a descending track with a high incidence angle was used and glacier velocity became more variable, increasing the combined SAR line-of-sight error to 3.26 cm. Low-error DInSAR images enabled the detection of a newly developed ~2.4 km grounding-line retreat associated with water intrusion behind a pinning point at the eastern margin of the glacier. Our results underscore that care must be taken to ensure that the low-error DInSAR results are used and that pinning points alter the grounding-line short-term migration and its long-term retreat.~~Tides modulated by atmospheric pressure were the major driver~~

~~of changes in the FZ with the correlation coefficient between DDInSAR and sea surface height displacements ranging from 0.81 to 0.94 for different RCM orbits. The lowest error (<0.1 cm in the SAR line-of-sight) occurred during the 'stable regime', when changes in glacier velocity were minimal, with ascending RCM tracks at incidence angles below 30°. During the 'unstable regime', the glacier velocity became more variable, and the error increased by up to 4 times. In summer, ice in the FZ flowed ~ 2.7-fold faster than the grounded section upglacier. We discovered a new ~ 2.4 km grounding line retreat associated with a pinning point at the eastern margin of the glacier. This rapid change is likely due to water intrusion and subglacial melt near the pinning point and shows how these bed features alter the grounding line short-term migration and its long-term retreat.~~

1. Introduction

Formatted: Normal

Marine-terminating glaciers, which drain ice masses from land to the ocean, have experienced dramatic changes ~~associated with a warming climate~~ in recent decades due to a warming climate, particularly in the Arctic, where temperatures are rising faster than the global average (Black & Joughin, 2022; Kochtitzky & Copland, 2022; Rantanen et al., 2022). ~~–~~Rising atmospheric and oceanic temperatures can cause these glaciers to accelerate, leading ~~Acceleration of these glaciers due to rising atmospheric and oceanic temperatures leads~~ to increased sea level rise and discharge of icebergs or ice islands into adjacent waters (~~IPCC, 2021~~ Morlighem et al., 2019; Wood et al., 2021; Carnahan et al., 2022; Holmes et al., 2025). Increased ice discharge and ice mass losses ~~Changes in the areal extent, velocity and calving dynamics~~ associated with Arctic glacier volume decrease, retreat, and deterioration were recently documented by Millan et al.~~,~~ (2017; 2023) and Van Wychen et al.~~,~~ (~~2016,~~ 2020). As a result of these changes, many glaciers located in Greenland and the Canadian Arctic shifted from marine to land~~-~~ terminating glaciers between 2000 and 2020 (Kochtitzky & Copland, 2022). To characterize and explore the stability of marine terminating glaciers, recent studies have focused on the boundary where glaciers transition from grounded to floating (e.g., Rignot et al., 2024; Kim et al., 2024), known as the grounding line. The grounding line exhibits dynamic behaviour, migrating with tides over short time scales (Freer et al., 2023) and advancing or retreating in response to changes in glacier dynamics over the long term (Milillo et al., 2022; Chartrand et al., 2024). Accurate mapping and monitoring of grounding-line dynamics are crucial for better understanding glacier retreat patterns and the processes that drive this retreat.

~~The satellite-based Double-Difference Interferometric Synthetic Aperture Radar (DDInSAR) method has been proven to be efficient for accurate monitoring of grounding line migration with a sequence of SAR images acquired at high temporal (sub-day to 4 days) and spatial (from sub-metre to a few metres) resolutions (Milillo et al., 2022; Rignot et al., 2024; Antropova et al., 2024; Kim et al., 2024).~~ The satellite-based Differential Interferometric Synthetic Aperture Radar (DInSAR) method has been proven to be highly effective for accurate monitoring of grounding-line migration, using SAR imagery with high temporal (1-6 days) and spatial (1 m to a few metres) resolution, along with consistent multi-temporal coverage over large areas ranging from tens to several hundreds of kilometres (Rignot et al., 2011; Milillo et al., 2017). Among the currently operational SAR

missions explored for DInSAR grounding-line applications, the RADARSAT Constellation Mission (RCM, C-band) has a 4-day acquisition cycle (Antropova et al., 2024; Gadi et al., 2025). This is comparable to COSMO-SkyMed (X-band) allowing 1 to 4 day revisits (Milillo et al., 2022; Rignot et al., 2024), and shorter than Sentinel-1 (C-band) with 6 to 12 day revisits (shorter with the A+B or A+C constellations) (Ramanath et al., 2025; Wild et al., 2025), TerraSAR-X (X-band) providing 11-day revisit (shorter with TanDEM-X) (Wild et al., 2018; Wild et al., 2025), and ALOS PALSAR (L-band) with a 46-day revisit (Rignot et al., 2011). The relatively short revisit time of RCM enables high phase coherence, while its C-band wavelength provides sensitivity to small vertical displacements, allowing reliable DInSAR measurements for grounding-line monitoring. The ~~D~~DInSAR method detects the differential ~~ice~~ tidal-flexure zone, hereafter referred to as the flexure zone ~~(FZ),~~ where the glacier surface flexur~~ees~~ with tides is captured at SAR data acquisition times. This zone, also referred to as the grounding zone in some studies (e.g., Fricker et al., 2009; Freer et al., 2023), spans from the inland limit of tidal flexure (i.e., the hinge line) past the grounding line to the seaward limit of flexure (i.e., hydrostatic equilibrium line), where hydrostatic equilibrium is reached and the ice tongue becomes completely buoyant. Nevertheless~~However~~, most recent ~~D~~DInSAR-based studies consider the hinge line as a proxy for the grounding line, so they tend to refer to the hinge line, and the bounds where it migrates over the tidal cycle, as the grounding line and grounding zone ~~(GZ)~~, respectively (Mohajerani et al., 2021; Chen et al., 2023; Ciracì et al., 2023; Rignot et al., 2024). To ensure clarity and consistency, hereafter, we use the terms 'flexure-zone ~~FZ~~ width~~span~~' (i.e., the along-glacier distance from the hinge line to the line of hydrostatic equilibrium) and '~~GZ span~~' "grounding-zone width' (i.e., the along-glacier distance from the most landward hinge line to the most seaward hinge line); ~~also referred to as 'grounding zone width' in~~ to conform with ~~the~~ recent DInSAR studies~~)~~. We also assume that the relative movements (e.g., short-term migration and long-term retreat) of the ~~D~~DInSAR-derived 'hinge line' and the actual 'grounding line' are equivalent, as their positions are strongly correlated (Rignot, 1996).

Recent DInSAR-based studies highlighted the complexity of grounding-~~-~~line migration with tidal cycles and explored the causes of this complexity, including glacier geometry, ~~the~~ underlying bed type, subglacial hydrology, and sea water intrusions (e.g., Mohajerani et al., 2021; Ciracì et al., 2023, Rignot et al., 2024; Kim et al., 2024), as well as the contributions of compressional and tensional strain components induced by ice-surface bending to the DInSAR signal (Rack et al., 2017; Wild et al., 2018). In addition, ~~D~~DInSAR-based observations showed that ~~GZ span~~grounding-zone width tends to be one to two orders of magnitude larger than predicted by the hydrostatic equilibrium equation (Chen et al., 2023, Milillo et al., 2022, Mohajerani et al., 2021). Since ~~GZs~~ grounding zones are associated with pronounced ice melt, this implies that the assumption that grounding lines are fixed over space and time made by many conventional numerical glacier/ice sheet models ~~are~~ is problematic (Ciracì et al., 2023; Rignot et al., 2024). ~~In order~~ Tto improve these models, ~~and to better understand glacier deterioration processes and long-term glacier retreat,~~ a detailed investigation of ~~the controls that drive grounding line migration~~ the drivers and glacier-system responses governing grounding-line migration over ~~a seasonal~~ short-term cycles and its long-term advance or retreat is required. The reliability of satellite-based observations used to monitor these processes should also be thoroughly evaluated..

Our study explores intra-annual changes in the Milne Glacier ~~FZ~~ flexure zone based on a combination of ~~RADARSAT Constellation Mission (~~RCM~~)~~ ~~D~~DInSAR-derived results, in ~~-~~situ and simulated datasets, and a numerical weather prediction model output ~~datasets~~. The objectives of this study are to:

- Delineate the Milne Glacier ~~FZ~~ flexure zone ~~over short-term migration cycles~~ using RCM data acquisitions from four different orbits, with a 4-day repeat interval within each orbit and about a 1-day interval between orbits, spanning from February 17, 2023 to September 17, 2024;
- Examine the relationship between ~~D~~DInSAR-derived ice~~-~~surface vertical displacement and displacement of sea surface height (DSSH), computed from simulated tides and in situ atmospheric pressure records together with modeled atmospheric pressure. We further ~~relate~~ assess this correlation across the four SAR orbits ~~to~~ with respect to the compressional and tensional strains caused by ice-surface bending in the flexure zone during two velocity ~~regimes~~periods:
  a) a ~~stable~~ steady ~~regime~~ period, when the in ~~-~~situ~~-~~measured Milne Glacier velocity did not change appreciably during winter~~,~~ and the DInSAR assumption of invariant velocities was met; and
  ~~-~~b) an ~~unstable~~ unsteady ~~regime~~ period, when velocity~~the~~ changes ~~in velocity~~ were evident, the glacier decelerated after summer peak velocity~~marked~~, and the DInSAR assumption of invariant velocities was violated.
- Explore ~~short-term FZ~~flexure-zone changes, including its ~~span~~width, its landward position (i.e., hinge line), and the ~~span~~ width of the ~~GZ~~ grounding zone over the study period with respect to ~~D~~DInSAR-derived surface displacements and glacier surface and bed geometry datasets.

In ~~-~~situ datasets of the Milne Glacier surface and bed geometry, as well as tidal observations, are used to interpret patterns in intra-annual flexure-zone~~FZ~~ migration.

Our results provide insight into ~~information about seasonal~~ short-term migration patterns of the grounding line based on its ~~D~~DInSAR-derived proxy, the hinge line, and help ~~to~~ elucidate ice deterioration processes that drive long-term grounding~~-~~line retreat ~~in the long term~~. By comparing steady and unsteady velocity periods, this study evaluates the reliability of DInSAR under varying flow conditions and offers new insight into how short-term glacier dynamics influence the interpretation of grounding-line positions derived from high-resolution multi-orbit RCM SAR imagery.

2 Study site and methods

2.1 Study site description

Milne Glacier is located on the northern coast of Ellesmere Island, the largest and northernmost island in the Canadian Arctic Archipelago (Fig. 1 inset map). The glacier is one of the major outlet glaciers of the 'Northern Ellesmere Icefield' (Millan et al., 2017) that discharges terrestrial ice into Milne Fiord. In the past, Milne Glacier was the central and most important glacier feeding the Milne Ice Shelf, the second largest remnant of the extensive Ellesmere Ice Shelf that collapsed in the early 20th Century (Mueller et al., 2017). The separation of Milne Glacier from the Milne Ice Shelf was accompanied by the formation and development of an epishelf lake (i.e., a layer of freshwater from summer ice melt and runoff that accumulates above

seawater between the shore and an ice shelf) first reported by Jeffries (1984). ~~Evidence of the Milne Ice Shelf thinning associated with the epishelf lake formation was observed from air photos acquired as early as the 1950s (Jeffries, 2002; Mortimer et al., 2012). Field observations of ice thickness and water profiling conducted in 1981 and 1983, respectively, confirmed the presence of an epishelf lake (Prager, 1983; Jeffries, 1985) although this term was not used until Veillette (2008).~~ The area of thin epishelf lake ice replacing the thick ice shelf increased from 5 km^2 to 17 km^2 between 1959 and 1984, reaching 28.5 km^2 by 2009 (Mortimer et al., 2012; Mueller et al., 2017). Currently, perennial epishelf lake ice and fragments of the former Milne Glacier ~~i~~Ice t~~T~~ongue that broke off the glacier between 2009 and 2011 are present within the ~22 km stretch between the present-day floating ice tongue and the ice shelf (Fig. 1 ~~in Antropova et al., 2024~~a).

The present-day intact floating ice tongue, located deep within Milne Fiord, is protected from drifting ice along the northern coast of Ellesmere Island (Mortimer et al., 2012). The floating ice tongue experiences moderate stresses due to tidal bending in the flexure zone. Milne Fiord is characterized by a semi-diurnal tidal regime with a relatively small tidal range, spanning from –20 cm to 21 cm over the observation period of this study, and a 14.8-day spring-neap-spring tidal cycle. However, atmospheric pressure also plays an important role in modulating sea surface height in the fjord (Wunsch & Stammer, 1997; Padman et al., 2003), further affecting the displacement of the ice tongue and increasing the stresses it experiences.

The glacier's transition zone between grounded ice and the floating ice tongue exhibited notable velocity fluctuations over the past decades.~~Changes were also observed in Milne Glacier's velocity near the grounding line, which~~ Ice velocity decreased from ~190 m yr^{-1} to ~100 m yr^{-1} between the 1990s and 2005 (Millan et al., 2017), increased to 120 - 140 m yr^{-1} in 2010, slowed down again to 80 - 100 m yr^{-1} from 2011 to 2015, and then accelerated to 140 - 160 m yr^{-1} between 2016 and 2020 (Van Wychen et al., 2020). Van Wychen et al. (2020) suggested that this cyclical behaviour may result from prominent bedrock features that modulate velocity where the glacier rests below sea level. In contrast, Antropova et al. (2024) noted that the post-2016 acceleration was preceded by the highest grounding-line retreat rate along the glacier's centerline between 2011 and 2018, suggesting the presence of feedback mechanisms between grounding-line retreat and upstream glacier acceleration.

The Milne Glacier grounding~~-~~line retreated by 3.1 km along the glacier's centre line from 1966 to 2023. The average rate of the grounding~~-~~line retreat was more than twice as high near the western margin (124 m yr^{-1}) compared to the centre (53 m yr^{-1}) of the glacier between 2011 and 2023.

Warming oceanic masses likely enhanced the grounding~~-~~line retreat in recent decades since variations in the grounding~~-~~line retreat rates were associated with changes in oceanic forcing (Antropova et al., 2024). Vertical thinning due to basal melt, was estimated at 15-32 m yr^{-1} between 2011 and 2019 (Bonneau et al., 2024) with a greater thinning rate near the glacier's deeper western side than at the shallower central and eastern edges. The glacier's vulnerability to oceanic warming is likely due to its bed geometry (Antropova et al., 2024). Milne Glacier's retrograde bed slope near the present-day grounding line makes the glacier susceptible to marine ice-sheet instability (Weertman, 1974; Schoof, 2007~~); Weertman, 1974),~~ a process where grounding~~-~~line retreat enhances glacier deterioration, which, in turn, triggers further retreat. This positive feedback loop may be underway currently~~,~~ and ~~will continue~~is expected to persist until the grounding line reaches a prograde bed slope roughly 1

km ~~further~~ up-glacier. Based on the glacier's 2011-2023 average retreat rate, this would occur in 2035.~~,~~ However, grounding-line retreat is inherently non-linear and governed by the complex interplay of glacier-specific and environmental controls. Reaching this slope ~~which~~ will help stabilize the glacier and inhibit further recession of its grounding line.

2.2 Data and methods

2.2.1 Processing of SAR data

~~Our datasets included satellite SAR and in-situ observations that provide information about the Milne Glacier FZ, the glacier surface and bed topography, ice velocity, and local tides.~~ We used ~~a sequence of~~ RCM single look complex (SLC) images with HH polarization, acquired in 'High Resolution 5m Mode' (MDA, 2021) from different orbits ~~during~~ in 2023–2024 (Table 1).~~,~~ ~~with~~This mode has a nominal resolution (i.e., theoretical resolution, which is based on radar system parameters) of 5 m and a swath width of 30 km. ~~(Table 1).~~ The native SLC pixel spacing is 1.4–2.8 m in the range direction and 2.4–2.8 m in the azimuth direction depending on the incidence angle (Table 1). The RCM SAR images were employed 1) to compute changes in the Milne Glacier surface, which allowed for flexure zone ~~delineation of~~ and ~~FZ~~/hinge line delineation and quantification of ~~displacement for the~~ floating ice tongue vertical displacement, and 2) to estimate ice velocities to compare with GNSS observations discussed in Section 2.2.3.

Table 1. Description of RCM dataset~~s~~ acquired between February of 2023 and September of 2024 for ~~the~~ Milne Glacier ~~FZ~~ flexure-zone (FZ) delineation~~s~~ and velocity ~~calculations~~estimates described in Section 2.2.3.

Relative orbit ID and derived results: flexure zone (FZ) and/or velocity (V)	Orbit pass: Des./ Asc.	Incidence angle (degrees)	SAR parameters for error calculations (Eq. 2): Incidence angle, Track angle[1] (degrees)	Raw image pixel size Range (m) x azimuth (m)	Period of data acquisitions yyyy.mm.dd (time UTC ± 1 min)	Number of FZ delineations
09 FZ, V	Des.	38.5-40.6 (Swath 12)	**39.5**, 230	2.4 × 2.6	2023.02.17 – 2024.03.23 (13:19)	42
43 FZ	Asc.	19.0-21.9 (Swath 1)	20.3, -58.9	1.4 × 2.4	2023.03.07 – 2024.03.17 (19:58)	27
53 V	Des.	52.7-54.1 (Swath 23)		2.8 × 2.8	2023.03.08 – 2024.03.26 (12:06)	–
58	Asc.	20.1-23.1	21.5,	1.4 × 2.4		25

Formatted: Font: Bold

Formatted: Font: Bold

FZ, V		(Swath 2)	-58.0		2023.03.12 – 2024.03.26 (20:06)	
73 V	Asc.	22.2-25.1 (Swath 3)		1.4 × 2.6	2023.03.13 – 2024.03.27 (20:13)	–
103 FZ	Asc.	26.3-28.9 (Swath 5)	27.5, -55.0	1.4 × 2.5	2023.03.11 – 2024.09.17 (20:30)	22

[1] Azimuth (clockwise from True North)
[2] The incidence angle of orbit 09 is 1.4 - 2 times greater than that of orbits 43, 58, and 103.

To delineate the ~~FZ~~flexure zone, the RCM images were processed using the ~~D~~DInSAR method (Rignot, 1996~~)), with further details described by Antropova et al. (2024)~~. This method reveals the surface displacement of the floating ice tongue along the SAR line-of-sight, by removing the effect of steady glacier flow, ~~through~~ by differencing two consecutive interferograms, under the assumption that the glacier velocity remains~~is~~ constant between SAR data acquisitions. The hinge line and the hydrostatic equilibrium line are then manually or automatically delineated by examining the landward and seaward ~~boundaries~~ limits of the fringe pattern in the DInSAR images representing ~~associated with glacier~~ the flexure zone. We used ~~the~~ GAMMA ~~software~~ (Werner et al., 2000) to compute the differences in the SAR phase and quantify changes in the surface height between data acquisitions. ~~The effect of topography was eliminated using 10 m resolution ArcticDEM (Porter et al., 2023).~~ Interferograms were computed for each pair of RCM data acquisitions with a 4-day interval. During processing, we applied 3 × 3 multilooking to reduce speckle, improve the signal-to-noise ratio and interferometric coherence, and reduce file sizes to facilitate phase unwrapping. After multilooking, the effective ground pixel spacing was approximately 9–10 m. Topographic phase removal and terrain correction were performed using the 10 m ArcticDEM dataset (Porter et al., 2023). Interferograms were unwrapped using the minimum-cost flow phase unwrapping algorithm described by Costantini (1998). During the initial unwrapping, the processing software automatically selected an arbitrary stable reference area. Then, ~~double~~ differential~~ee results~~ interferograms were calculated at 10 m resolution (i.e., the final spatial resolution of DInSAR images used for flexure zone delineations) ~~for interferogram pairs~~and the corresponding unwrapped results represented by three consecutive data acquisitions (over 8 days) or four data acquisitions (over ≥12 days) if there was a gap between data acquisitions. The final calibration of ~~.~~the SAR line-of-sight displacement was conducted along three transects (Fig. 1, described below) using an automated script. Values were divided by the cosine of the incidence angle and additionally calibrated to the mean values of the grounded portions of the transects for each DInSAR image from orbits 09 and 103. Phase jumps exceeding 2 cm (i.e., a more conservative threshold than half of the RCM C-band wavelength) were corrected for all orbits.

The western and eastern ~~FZ~~ flexure-zone boundaries were often affected by noise. These areas of low interferometric coherence typically occur due to strong velocity gradients, shear, ice deformation, and rotation as glacier velocities decrease from the centre toward the lateral margins as a result of lateral drag (Forster et al., 1999; Mannerfelt et al., 2025). These processes

contribute to ice weakening and a reduction in stiffness in the lateral shear zone (e.g., a fivefold reduction in Young's modulus was reported by Wild et al., 2025). This interpretation is supported by our in situ observations and high-resolution imagery demonstrating extensive crevassing in this zone, particularly along the western margin of Milne Glacier, where a tributary glacier further enhances these processes. ~~due to extensive~~The resulting loss of coherence in the flexure-zone's western and eastern boundaries ~~crevassing, which~~ prevented their reliable delineation and the use of the entire area of the ~~FZ~~ flexure zone for our analysis. Instead, changes to the ~~FZ~~ flexure zone were quantified as follows.

The ~~FZ~~ flexure-zone boundaries were manually delineated using geographic information system (GIS) software and analysed along three transects on the western, central and eastern sides of the glacier, denoted by subscripts: $_W$, $_C$, $_E$, respectively (Fig. 1). Each of these transects ha~~s~~ve known surface and bed topography (Fig. 1 a and Fig. 10 in the Results section) from airborne and in ~~-~~situ radar observations (CReSIS, 2021; Antropova et al. 2024). The transects start up-glacier at an arbitrary fixed point (A) at km 32 along the 2014 IceBridge radar transect. In a given DInSAR image (denoted by numbered subscripts), t~~T~~he three transects cross the hinge line at point B and the hydrostatic equilibrium line at point C. We used the following variables to characterize the temporal evolution of the ~~FZ~~flexure zone:

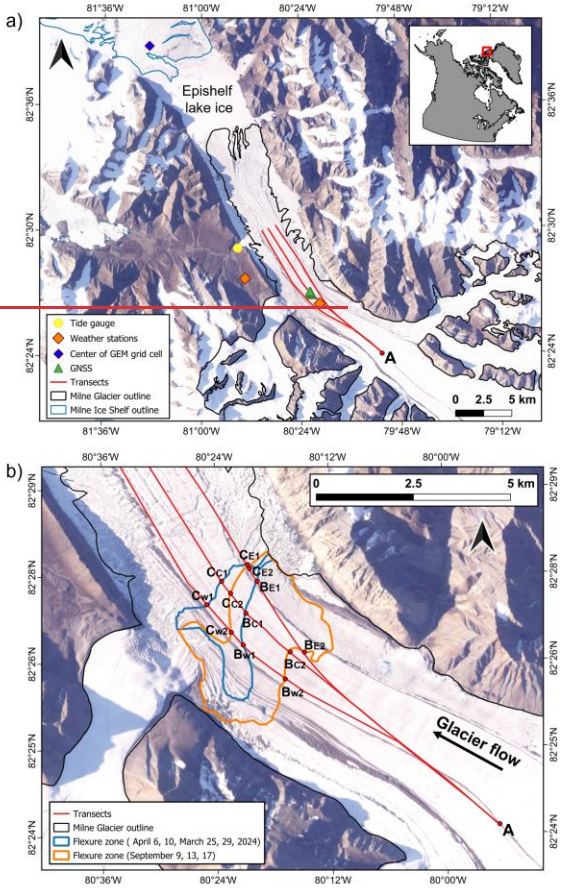
- flexure-zone width (e.g., for DInSAR image 1, distance between B_{W1} and C_{W1} in Fig. 1);
- surface displacement in the vertical direction;
- distance to hinge line from the fixed point A (e.g., distances between A and B_{W1}, A and B_{C1}, and A and B_{E1} in Fig. 1);
- ~~GZ~~ grounding-zone ~~span~~ width (i.e., the distance along the glacier between the most landward and most seaward hinge~~-~~ line delineations based on all DInSAR images over the entire ~~period of our~~ observation period~~s~~).~~,~~ ~~e.g.,~~For illustrative purposes, the grounding zone is shown by the distance between B_{W1} and B_{W2} in Fig. 1, based on DInSAR image 1 and 2 associated with data acquisitions in March-April 2024 and September 2024. ~~in Fig. 1);~~
- ~~FZ span (e.g., distance between B_{W1} and C_{W1} in Fig. 1);~~
- ~~surface displacement in the vertical direction (i.e., the SAR line-of-sight displacement from the unwrapped interferograms, which was corrected for phase discontinuities along the transects and divided by the cosine of the incidence angle).~~

Formatted: Not Superscript/ Subscript

Formatted: Not Superscript/ Subscript

Formatted: Not Superscript/ Subscript

Formatted: List Paragraph, Bulleted + Level: 1 + Aligned at: 0.63 cm + Indent at: 1.27 cm


a)
81°36'W
81°00'W
80°24'W
79°48'W
79°12'W
82°36'N
82°30'N
82°24'N
Epishelf
lake ice
A
Tide gauge
Weather stations
Center of GEM grid cell
GNSS
Transects
Milne Glacier outline
Milne Ice Shelf outline
0 2.5 5 km
b)
80°36'W
80°24'W
80°12'W
80°00'W
82°29'N
82°28'N
82°26'N
82°25'N
82°24'N
0 2.5 5 km
CE1
CC1
CE2
BE1
Cw1
CC2
BC1
Cw2
BE2
Bw1
BC2
Bw2
Glacier flow
A
Transects
Milne Glacier outline
Flexure zone (April 6, 10, March 25, 29, 2024)
Flexure zone (September 9, 13, 17)

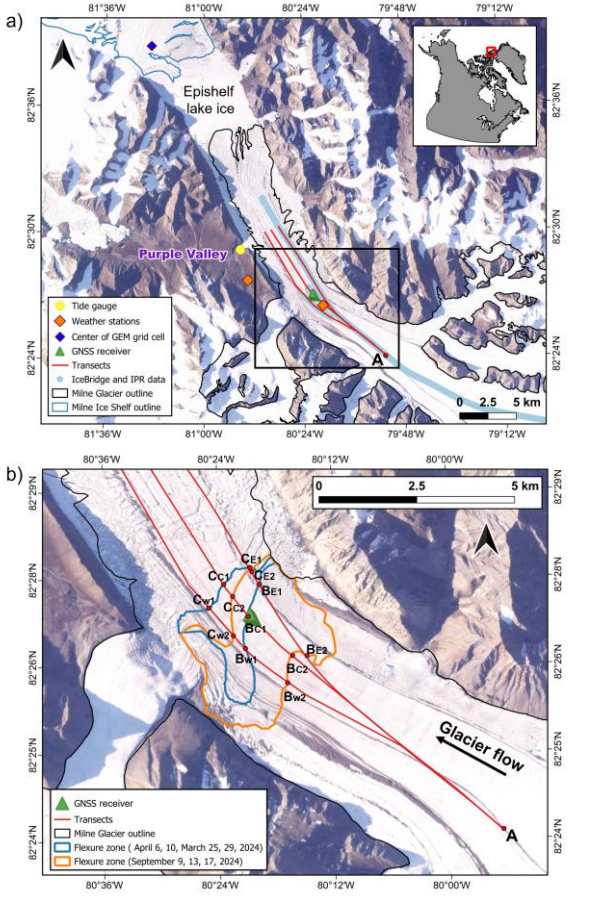


Figure 1: Study site. a) Locations of Milne Glacier, in ~~-~~situ instrumentation, and Global Environmental Multiscale (GEM) grid cell centre. b) Milne Glacier tidal-flexure zone ~~FZ~~ with two examples of its delineation based on SAR images acquired (1) between March 25 and April 10, 2024 (blue polygon) and (2) September 9 and 17, 2024 (orange polygon) shown over a Planet image ~~(Planet Team, 2017)~~ acquired on August 12, 2024 (Image © [2024] Planet Labs PBC). Flexure-zone~~Z~~ variables explored in this study ~~and~~ are computed along the western, central, and eastern transects (subscript W, C, and E) shown in red (through points A, B and C). These variables include ~~are~~: 1) distance to hinge lines (A to B_{W1}, A to B_{C1}, A to B_{E1} for ~~f~~Flexure zone~~Z~~ in DInSAR image 1, ~~(~~blue polygon~~,)~~ and A to B_{W2}, A to B_{C2}, A to B_{E2} for flexure zone~~FZ~~ in DInSAR image 2, ~~(~~orange polygon), 2) ~~span~~ width of the two Flexure zone~~Z~~s (B_{W1} to C_{W1}, B_{C1} to C_{C1}, B_{E1} to C_{E1} and B_{W2} to C_{W2}, B_{C2} to C_{C2}, B_{E2} to C_{E2}), 3) Grounding-zone~~Z~~ ~~span~~ width (B_{W1} to B_{W2}, B_{C1} to B_{C2}, B_{E1} to B_{E2}), and 4) surface displacement height of the floating ice.

~~The vertical component of DDInSAR-derived surface displacement of the floating part of the glacier was analysed with respect to the changes in sea surface height due to tides and atmospheric pressure (Rignot et al., 2024).~~

2.2.2 Analysis of tides and reconstruction of ice-surface height timeseries

The vertical component of DInSAR-derived surface displacement of the floating part of the glacier was analysed with respect to the changes in sea surface height due to tides and atmospheric pressure. We used tidal constituents derived from in -situ tidal observations recorded every 6 seconds with an RBR Duet datalogger deployed at ~10 m depth in a lateral bay on the western side of Milne Fiord (i.e., tide gauge location in Fig.1 a) ~~collected~~ between September 3, 2016 and July 4, 2017 ~~(see further details provided in Antropova et al., 2024)~~ to simulate tides at a 1-minute interval for the period of SAR observations using the T_TIDE~~t-tide~~ toolbox (Pawlowicz et al., 2002). Simulated tide heights were corrected ~~for~~ by adding the inverse barometer effect (IBE) (Wunsch & Stammer, 1997; Padman et al., 2003), while ocean tide loading on the Earth's crust was neglected, as it has a relatively minor impact (Wild et al., 2025).~~,~~ We us~~ed~~ing the atmospheric pressure data recorded every 30 minutes by our in -situ weather stations (Fig. 2 c)~~. To calculate the sea surface height (SSH), G~~gaps in the in situ pressure records (i.e., July 9–21, 2023, with no associated DInSAR images, and July 22–September 17, 2024, with one DInSAR image) were filled ~~with~~ using the Global Environmental Multiscale (GEM) model ~~data~~ output (Buehner et al., 2015). The GEM model-based data at a 1-hour interval were extracted for a GEM grid cell of about 15 km × 15 km centred at 82.6477°N, 81.3225°W on the Milne Ice Shelf about 9 km to the northwest of the glacier terminus, to avoid the influence ~~so the effect~~ of higher elevations in grid cells closer to~~near~~ the grounding line ~~was avoided~~ (Fig. 1). Both~~,~~ air temperature and surface pressure were in ~~a~~ good agreement with in -situ observations (Fig. 2). In particular, the correlation between the GEM model and in situ atmospheric pressure records used for IBE calculations was 0.96, with a root mean squared error (RMSE) of 3.6 hPa. To calculate the IBE over the entire observation period, we assumed that a 1 hPa change in atmospheric pressure results in a corresponding -1 cm change in sea level (Wunsch & Stammer, 1997; Padman et al., 2003). This correction was linearly interpolated to a 1-minute interval and then added to the simulated tides to compute the sea surface height (SSH). The SSH computed using T_TIDE showed a higher correlation (0.96 vs. 0.93) and lower RMSE (3.4 cm vs. 4.6 cm) than the independent tidal model GR1kmTM (Howard and Padman, 2021) when compared with repeated in situ tidal observations collected in July 2023 (Fig. A1). This supports the choice of the T_TIDE algorithm for our analysis. DSSH, the difference in SSH for each ~~D~~DInSAR ~~result~~image, was calculated by subtracting the SSH values at the times of SAR data acquisition, consistent with the ~~D~~DInSAR subtraction. We assessed the relationship between DSSH and ~~D~~DInSAR-derived surface height displacement of the freely floating ice tongue (i.e., mean values calculated from 44 km downfjord along the three transects in Fig. 1) based on the correlation coefficient, the root mean squared error (RMSE), and bias.

To explore the origin of the newly developed notch along the eastern margin, we tested the hypothesis that it appears in DInSAR images associated with SAR acquisitions during periods of high SSH, suggesting that seawater intrudes farther inland and results in ice ungrounding around a pinning point. We calculated the minimum and maximum SSH values, as well as the

Formatted: Normal

standard deviation, for each DInSAR result associated with three or four SAR data acquisitions. These values were then divided into two groups corresponding to: (1) DInSAR results without the notch and (2) DInSAR results with the newly developed notch present, to test whether SSH differs significantly between the groups.

Then, we also reconstructed the ice surface height timeseries by least square fitting of our DInSAR displacements using all 59 tidal constituents computed with the T_TIDE algorithm (Pawlowicz et al., 2002). The coefficients for each harmonic component were estimated using a regularized least-squares approach assuming a ~~single~~ multifrequency harmonic function as follows:

$$d(t) = \sum_{j=1}^{N} [a_j \sin(\omega_j t) + b_j \cos(\omega_j t) + cH(t)] \quad (1)$$

where ω_j is the circular frequency corresponding to j^{th} tidal constituent, $H(t)$ is the time-dependant IBE component, and a_j, b_j, and c are the least squares fitting coefficients (Appendix B), t is time of SAR data acquisitions. In (1) $j = 1$ corresponds to the most dominant tidal constituent and $j = N = 59$ corresponds to the least dominant tidal constituent.

2.2.3 Assessment of uncertainties in flexure-zone delineations due to velocity variability and ice bending, , and SAR viewing geometry

To assess uncertainties in the flexure-zone delineations, we estimated the errors introduced into the computed SAR line-of-sight vertical surface displacement by velocity variability and by ice-surface extension and compression due to tidal bending. To investigate the effect of velocity variability on the grounding-line migration, we split our DInSAR datasets from all orbits into two periods associated with steady and unsteady glacier velocity periods (Fig. 2 a) for the period of SAR data acquisitions. To define these two flow periods, we used in situ-measured and SAR-derived glacier velocities in the flexure zone supported by air temperature observations. In situ velocities along the central transect were obtained with GNSS receivers (Garbo, 2024) installed near the grounding line (Fig. 1) to record positional information between July 2022 and July 2024. The instruments recorded positional information for three hours daily (i.e., 16:00 – 19:00), close to the SAR data acquisition times from orbits 43, 58, and 103, and with a larger time gap for orbit 09), yielding the GNSS position with an error of about 1.5 cm after static mode precise point positioning processing (NRCan, 2024). The final GNSS position was represented by the mean latitude and longitude values stabilized between 18:00 and 19:00 UTC, which was close to the SAR acquisition times for orbits 43, 58, and 103, but involved a larger time gap for orbit 09. Thus, the GNSS measurements likely captured a more representative tidal signal for orbits 43, 58, and 103 than for orbit 09. The observed distances between the GNSS positions were converted to daily velocities (Fig. 2 a). The missing GNSS records (10.5% of the total records within the analysed periods) at the end of the unsteady period and beginning of the steady period in 2024 were linearly interpolated from neighbouring observations and compared against SAR-derived velocity. The SAR-derived Milne Glacier velocity, averaged within a 3x3 pixel window at the GNSS receiver location (Fig. 1), is shown in Fig. 2a. To estimate the velocity, RCM SAR data acquired from four orbits (i.e.,

Formatted: Not Highlight
Formatted: Not Highlight
Formatted: Not Highlight

relative orbits: 09, 53, 58, and 73; Table 1) were employed to compute ascending and descending range and azimuth speckle offset products in GAMMA (Werner et al., 2000). Then, 3D displacement time series were derived from a set of linear equations using inverses (Samsonov et al., 2021). The interpolated values for the missing GNSS records agreed within ±0.01 md^{-1} with SAR-derived velocities. The SAR-derived velocities demonstrated a surprising spike in January–February 2024 (Fig. 2 a). This spike coincided with a rise in air temperature and likely represented real glacier acceleration. However, because the GNSS receiver ran out of battery and did not record in situ measurements during this period, these records were excluded from the velocity variability analysis.

The steady and unsteady periods were defined based on the glacier velocity strictly within the period of DInSAR data acquisitions to explore the effect of velocity variability on our DInSAR-derived results and do not necessarily represent annual patterns glacier dynamics. The steady period was defined as a period of invariant and low glacier velocity of about 0.4 m d^{-1} (SAR data acquisitions from February to May, 2023 and 2024, a period highlighted in blue in Fig. 2 a, b), which was predominantly associated with winter time and low air temperatures. Conversely, the unsteady period had changing velocity values that decreased from 0.6 m d^{-1} to 0.4 m d^{-1} (SAR data acquisitions from September to December 2023, a period highlighted in orange in Fig. 2 a, b), following a period of positive air temperatures and pronounced glacier acceleration in July and August (Fig. 2).

Formatted: Superscript

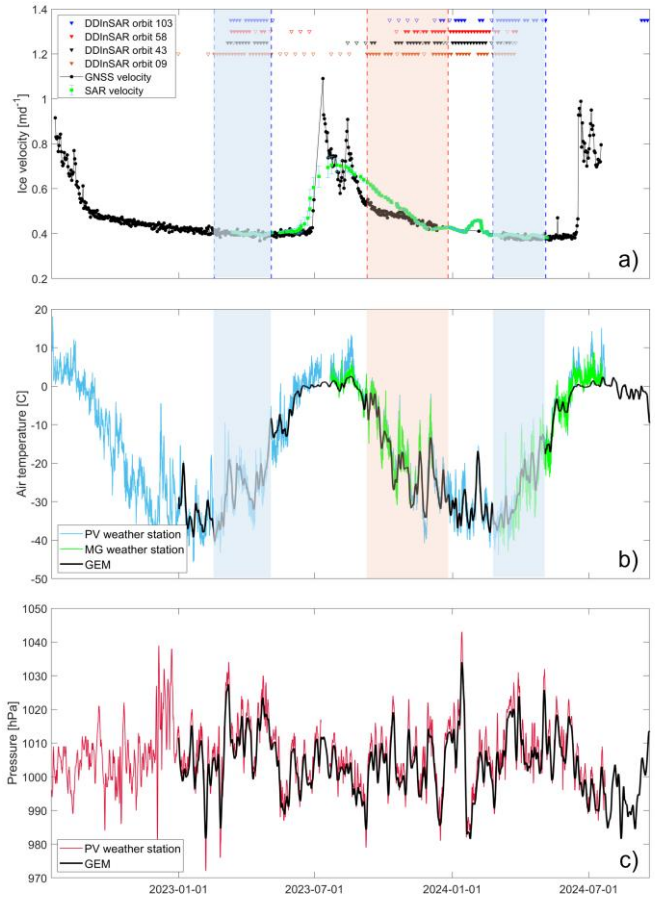


Figure 2: Milne Glacier ice velocity and meteorological observations. a) Daily ice velocity measured with GNSS receivers (black line) and calculated from SAR data (green line) in the flexure zone. b) Air temperature recorded on Milne Glacier (MG), in Purple Valley (PV), and retrieved from the GEM model. c) Barometric pressure recorded in Purple Valley, overlayed with GEM data, used to correct SSH. The winter SAR observation block associated with a steady glacier period, highlighted in blue, corresponds to relatively steady and low velocity values of 0.4 m d^{-1}. The fall SAR observation block associated with an unsteady period, highlighted in orange, corresponds to velocity values decreasing from 0.6 m d^{-1} to 0.4 m d^{-1}. SAR data acquisition times for four different orbits are shown with triangles: filled if flexure zone delineation was made, or empty if not, due to low coherence.

The correlation between DSSH and DInSAR-derived height was calculated for both the steady and unsteady periods and analysed with respect to glacier acceleration computed for the corresponding SAR data acquisition times. Acceleration was calculated as a local slope for five GNSS velocity records within a ±2-day time window centred on the day of each SAR data acquisition used in the DInSAR processing.

The error introduced to the line-of-sight surface displacement due to varying ice velocity between SAR data acquisitions in the computed DInSAR displacement, was assessed by calculating the absolute line-of-sight horizontal error, ε_{LOShV}:

$$\varepsilon_{LOShV} = |\Delta D \times cos\gamma| \quad (2),$$

where ΔD is the GNSS-derived difference in glacier displacement between the first and the second SAR image pairs used for the DInSAR computations, γ is the angle between the 3D-vectors of glacier velocity (taking into account the glacier flow heading of 317.7° with respect to True North and the glacier surface tilt of 3.5° in the flexure zone) and SAR line-of-sight for each orbit (taking into account the incidence and track angles shown in Table 1) calculated based on Eq. 1 in Samsonov (2024).

To assess the SAR line-of-sight error resulting from ice extension or compression due to tidal bending, we applied the elastic model described by Rack et al. (2017), using the mean ice thickness of the grounding zone along the central and western transects (i.e., 200.5 m and 225.6 m, respectively). We assumed an elastic Young's modulus of 1.5 GPa, which is consistent with Rack et al. (2017) and is close to values reported for glacier flexure zones (Wild et al., 2017, 2025). The maximum horizontal ice-surface deformation due to extension or compression (at a distance of 640.5 m and 699.5 m from the grounding line along the central and western transects, respectively) was modeled based on SSH at the times of SAR data acquisition. We then calculated the differential horizontal ice-surface deformation due to bending, consistently with the DInSAR image differencing. The absolute line-of-sight error due to bending, ε_{LOShB}, was calculated as follows:

$$\varepsilon_{LOShB} = |\Delta B \times cos\beta| \quad (3),$$

where ΔB is the horizontal ice surface deformation due to ice extension or compression, β is the angle between the 3D-vectors of glacier tangent line and SAR line-of-sight for a corresponding orbit. Our modeled maximum slope angle of the glacier tangent line with respect to the neutral position (for a maximum SSH of ±0.5 m) was 0.02°; therefore, we assumed that $\beta \approx \gamma$.

The uncertainty of the delineated hinge-line positions was assessed based on the sum of the computed line-of-sight errors arising from variations in ice velocity and ice bending. This combined error was expressed as a fraction of a SAR fringe, representing a vertical displacement of half the wavelength (i.e., 2.75 cm for RCM). To estimate the horizontal extent corresponding to a fraction of a SAR fringe, the typical fringe width along the central transect was calculated from the DInSAR images used for flexure-zone delineation. A Laplacian filter was applied to the DInSAR images to enhance fringe edges, after which fringe widths were computed for all images and the mean, median, and mode values were determined. Horizontal uncertainties were then calculated as fractions of the typical fringe width along the transect, represented by the median value.

~~Then, we reconstructed the ice surface height timeseries by least square fitting of our DDInSAR displacements with a single-frequency harmonic function as follows:~~

Formatted: Not Highlight
Formatted: Not Highlight
Formatted: Not Highlight
Formatted: Not Highlight
Formatted: Not Highlight
Formatted: Not Highlight
Formatted: Not Highlight

$$d(t) = a_1 \sin(\omega t) + a_2 \cos(\omega t) + a_3 H(t) \quad (1)$$

where ω is the circular frequency corresponding to the dominant semidiurnal M2 tidal constituent, $H(t)$ is the time-dependant IBE component, and a_i (i = 1, 2, 3) are the least squares fitting coefficients (Appendix A), t is time of SAR acquisitions. We considered two variants of the fitting function: 1) tide-based only (i.e., $a_3 = 0$) and 2) tide-based plus IBE term (i.e., $a_3 \neq 0$). We also explored tidal conditions associated with a new up-glacier notch in the FZ along the eastern transect in detail. We used SSH associated with SAR image acquisition times to calculate the minimum and maximum SSH values, and standard deviation, for each of our DDInSAR results. To characterize the tides associated with notch presence, we calculated average values of these statistics for two groups of DDInSAR grounding line delineations: 1) without the notch and 2) with the new notch present.

To investigate the seasonal effect on the grounding line migration, we split our DDInSAR datasets from all orbits into two periods associated with stable and unstable glacier velocity regimes (Fig. 2 a) for the period of SAR observations. To define these two flow regimes, we used in-situ measured and SAR-derived glacier velocities in the FZ supported by air temperature observations. In-situ velocities were obtained with GNSS receivers (Garbo, 2024) installed near the grounding line (Fig. 1) to record positional information between July 2022 and July 2023. The instruments recorded positional information for three hours daily yielding the GNSS position with an error of about a 1.5 cm after static mode precise point positioning processing (NRCan, 2024). The observed distances between the GNSS positions were converted to daily velocities (Fig. 2 a).

RCM SAR data acquired from four orbits (i.e., relative orbits: 9, 53, 58, and 73; Table 1) were employed to compute ascending and descending range and azimuth speckle offset products in the GAMMA software (Werner et al., 2000). Then, 3D displacement time series were derived from a set of linear equations using inverses (Samsonov et al., 2021). The Milne Glacier velocity represented by the SAR line-of-sight displacement at the GNSS receiver location (Fig. 1) is shown in Fig. 2a. The GNSS-derived velocities agreed well with our SAR-derived results.

The stable and unstable regimes were defined based on the glacier velocity strictly within the period of SAR observations to explore the effect of velocity on our DDInSAR results and don't necessarily represent general patterns in year-round glacier dynamics. Thus, the stable regime was defined as a period of invariant and low glacier velocity of about 0.4 m d^{-1} (SAR observations from February to May, 2023 and 2024, a period highlighted in blue in Fig. 2 a, b), which was predominantly associated with winter time and low air temperatures. Conversely, the unstable regime had changing velocity values that decreased from 0.6 m d^{-1} to 0.4 m d^{-1} (SAR observations from September to December 2023, a period highlighted in orange in Fig. 2 a, b) and followed the summer when positive air temperatures caused ice melt, triggering pronounced glacier acceleration in July and August.

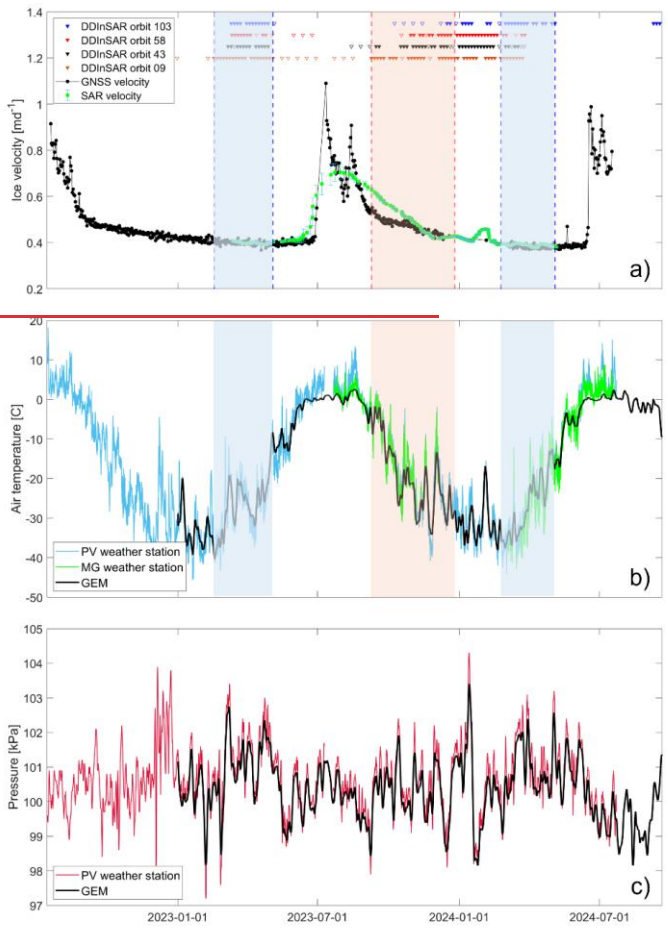


Figure 2: Milne Glacier ice velocity and meteorological observations. a) Daily ice velocity measured with GNSS receivers (black line) and calculated from SAR data (green line) in the FZ. b) Air temperature recorded on Milne Glacier (MG), in Purple Valley (PV), and retrieved from the GEM model. c) Barometric pressure recorded in Purple Valley, overlayed with GEM data, used to correct SSH. The glacier stable regime, highlighted in blue, corresponds to relatively steady and low velocity values of 0.4 m d^{-1}. The unstable regime, highlighted in orange, corresponds to velocity values decreasing from 0.6 m d^{-1} to 0.4 m d^{-1}. DDInSAR observations are shown with triangles: filled if FZ delineation was made, or empty if not, due to low coherence.

~~The correlation between DSSH and DDInSAR-derived height was calculated for both the stable and unstable regimes and analysed with respect to glacier acceleration computed for the corresponding SAR acquisition times. Acceleration was calculated as a local slope for five GNSS velocity records within a ±2-day time window centred on the day of each SAR acquisition used in the DDInSAR processing. A few missing GNSS records at the end of the unstable regime and beginning of the stable regime in 2024 were linearly interpolated from neighbouring observations.~~

~~The error introduced to the line-of-sight surface displacement due to varying ice velocity between SAR acquisitions in the computed DDInSAR displacement, was assessed by calculating the absolute line-of-sight horizontal error, ϵ_{LOSh},:~~

$$\epsilon_{LOSh} = |\Delta D \times cos\gamma| \quad (2),$$

~~where ΔD is the GNSS-derived glacier difference in glacier displacement between the first and the second SAR image pairs used for the DDInSAR computations, γ is the angle between the 3D vectors of glacier velocity (taking into account the glacier flow direction of 317.7° with respect to the north direction and the glacier surface tilt of 3.5° in the FZ) and SAR line-of-sight for a corresponding orbit (taking into account the incidence and track angles shown in Table 1) calculated based on Eq. 1 in Samsonov (2024).~~

2.2.4 Analysis of grounding-line migration and grounding-zone width

~~FZ~~ Flexure-zone variables such as distance from point A (Fig. 1) to the hinge line and the ~~FZ~~ flexure-zone width ~~span~~ along the three transects (Fig. 1) were ~~analysed~~examined with respect to glacier geometry and SAR-derived velocities over period ~~of DDInSAR-derived surface displacement as well as bed~~observations. In particular, bed and surface slopes retrieved from the airborne IceBridge radar data recorded in 2014 and ground-based ice penetrating radar (IPR) transects collected between 2016 and 2023 (Fig. 1, details described in Antropova et al., 2024) were employed. The surface elevation derived from the airborne and ground-based radar datasets was also compared against ArcticDEM (Porter, Claire, et al., 2023), a digital elevation product based on optical stereo imagery collected between 2008 and 2021 over Milne Glacier.

The distance from point A to the hinge line (B) was calculated for all orbits to investigate patterns of landward and seaward grounding-line migration. The Milne Glacier ~~GZ span~~grounding-zone width for the entire period of observations (2023 - 2024) was calculated as the~~a~~ difference between the maximum and minimum distances from point A to the most seaward and landward DInSAR-derived hinge lines, respectively, along the three transects ~~from our DDInSAR datasets~~ (e.g., max |A $B_{W_{max}}$| – min |A $B_{W_{min}}$| for the western transect). These results were compared with grounding-zone width derived from DInSAR images from orbits 43 and 103 within the steady period, which are associated with the lowest line-of-sight errors due to velocity variability and tidal bending and are therefore considered the most reliable. In addition, we assessed the theoretical ~~span~~ width of the grounding zone~~GZ~~ (ΔL) for the three transects shown in Fig. 1 with the known surface and bed geometry based on the following equation (Tsai & Gudmundsson, 2015):

$$\Delta L = \Delta h_{high}\left((\alpha-\beta)\frac{\rho_i}{\rho_w}+\beta\right)^{-1} + \Delta h_{low}\left(\frac{\alpha\rho_i}{\rho_w\left(1-\frac{\rho_i}{\rho_w}\right)}+\beta\right)^{-1} \quad (43),$$

Formatted: Heading 2

Formatted: Not Highlight

Formatted: Not Highlight

Where Δh_{high} and Δh_{low} are the highest (0.50 m) and lowest (-0.44 m) ~~tidal heights corrected for the inverted barometric pressure~~SSH during the period of observations, α and β are surface and bed slopes calculated over the entire distance of available in ~~-~~situ IPR observations and from 38 km to 42 km of the IceBridge transect (Fig. 10), ρ_i and ρ_w are ice (917 kg/m^3) and water densities (1025.4 kg/m^3, an average value for 100-200 m depth in Milne Fiord), respectively. This equation was derived by Tsai and Gudmundsson (2015) based on prograde bed geometry and was later applied to both retrograde and prograde bed geometries (e.g., Chen et al., 2023), assuming negligible bending stresses at the ice surface ~~(e.g., Chen et al., 2023)~~. The calculated theoretical ~~span~~ width of the ~~GZ~~ grounding zone was compared against the SAR-derived one. ~~In addition~~Finally, ~~radar~~IPR-derived bed topography and SAR-derived velocity in the ~~GZ~~ grounding zone w~~ereas~~ used to interpret processes of ice ~~migration~~ dynamics and deterioration in this critical zone.

3. Results

3.1 DInSAR results

We delineated 116 ~~ice~~ flexure zones ~~FZs~~ from four different orbits (Fig. 3 a) using the ~~D~~DInSAR technique applied to three or four sequential RCM ~~images~~ SAR scenes acquired four days apart ~~from four different orbits~~. Our delineations revealed short-term fluctuations and systematic changes in the ~~FZs~~flexure zones, with the zone's ~~span~~ width ~~(i.e., distance~~ along~~- the~~ glacier flow~~)~~ varying from 46 m to ~2.9 km (Table 2). The result~~ings for~~ minimal ~~FZ~~ flexure-zone ~~span~~ widths were consistent among the four orbits: with the smallest values along the eastern transect, followed by the values for the central transect, and the ~~highest~~ largest values along the western transect. M~~The m~~aximum ~~FZ~~ flexure-zone ~~span~~ width values were consistently higher for the western transect, but values for the eastern transect were often larger than for the central transect. ~~This suggests that ice flexes with tides differently along the three transects, likely due to a distinctive bed geometry and ice thickness.~~

Table 2. Milne Glacier ~~FZ~~ flexure zone ~~span~~ widths over the period of observations.

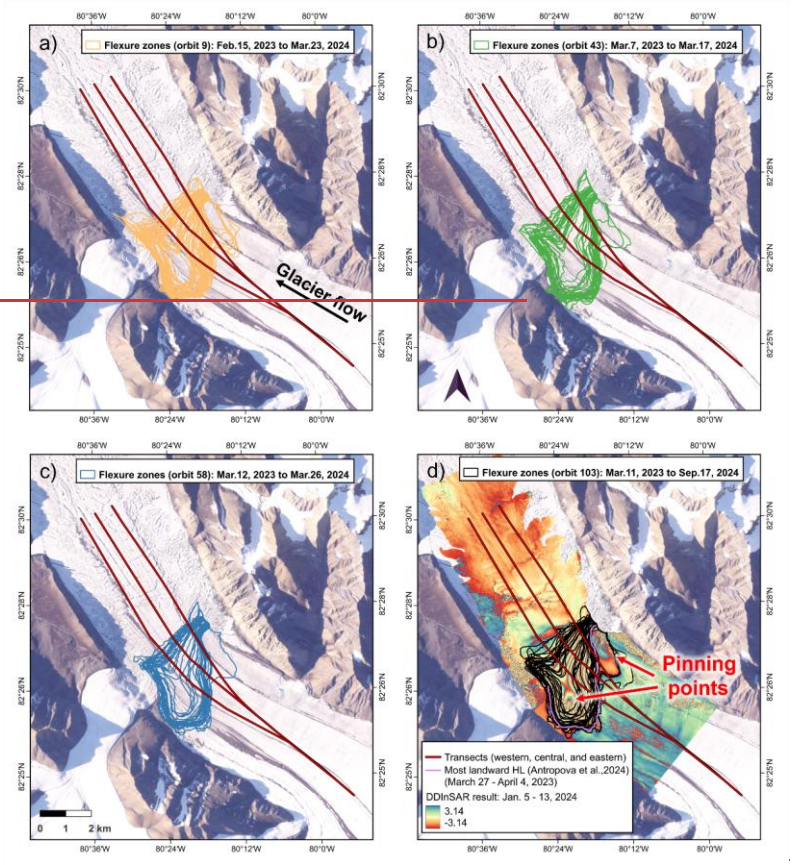
Relative orbit ID	Western transect, min – max (m)	Central transect, min – max (m)	Eastern transect, min – max (m)
09	641 – 2873	485 – 2222	46 – 2422
43	862 – 2760	548 – 2223	188 – 2153
58	888 – 2896	620 – 2395	358 – 2522
103	770 – 2744	561 – 2125	323 – 2574

~~Our~~ Hinge lines derived from ~~D~~DInSAR ~~results~~images~~, based on acquisitions~~ between February and September 2023, re-confirmed that the hinge line was asymmetric with a pronounced notch in the glacier western margin, as reported by Antropova et al. (2024; Fig. 3). However, several interferograms between October 2023 and September 2024 exhibited a new notch in the ~~FZ~~ flexure zone pointing up-glacier at the glacier's eastern margin. As a consequence, the glacier flexure zone~~FZ~~'s eastern

Formatted: Normal

edge, that had a much lower average ~~hinge~~ grounding line retreat rate (29 m yr^{-1}) than its central (53 m yr^{-1}) and western (124 m yr^{-1}) regions between 2011 and 2023 (Antropova et al., 2024), experienced rapid changes ~~during the last part of our intensive~~toward the end of the current observation period. The grounding-line retreat ~~Similar to the western side of the glacier, ice deterioration~~ on the eastern side occurred around a pinning point associated with a "bull's-eye" pattern in the ~~D~~DInSAR interferograms (Fig. 3d, and Fig. A2), similar to the bull's-eye pattern near the western side of the glacier observed by Antropova et al. (2024). The grounding line shifted up-glacier by 1 km compared to the most landward position observed during March 27-April 4 2023 in our previous study (i.e., Antropova et al., 2024; Fig. 3 d), and exhibited a shift of approximately 690 m along the eastern transect between the most landward hinge-line positions derived from all DInSAR images with and without the notch in this study. This shift was even more pronounced farther east, where the notch advanced landward by 2.5 km compared to the last reported position and by 2.4 km (measured parallel to the eastern profile) for observations with and without the notch during the period covered by this study.~~)~~.

Formatted: Not Highlight


a)
Flexure zones (orbit 9): Feb.15, 2023 to Mar.23, 2024
Glacier flow
b)
Flexure zones (orbit 43): Mar.7, 2023 to Mar.17, 2024
c)
Flexure zones (orbit 58): Mar.12, 2023 to Mar.26, 2024
0 1 2 km
d)
Flexure zones (orbit 103): Mar.11, 2023 to Sep.17, 2024
Pinning points
Transects (western, central, and eastern)
Most landward HL (Antropova et al.,2024) (March 27 - April 4, 2023)
DDInSAR result: Jan. 5 - 13, 2024
3.14
-3.14
80°36'W
80°24'W
80°12'W
80°0'W
82°30'N
82°28'N
82°26'N
82°25'N

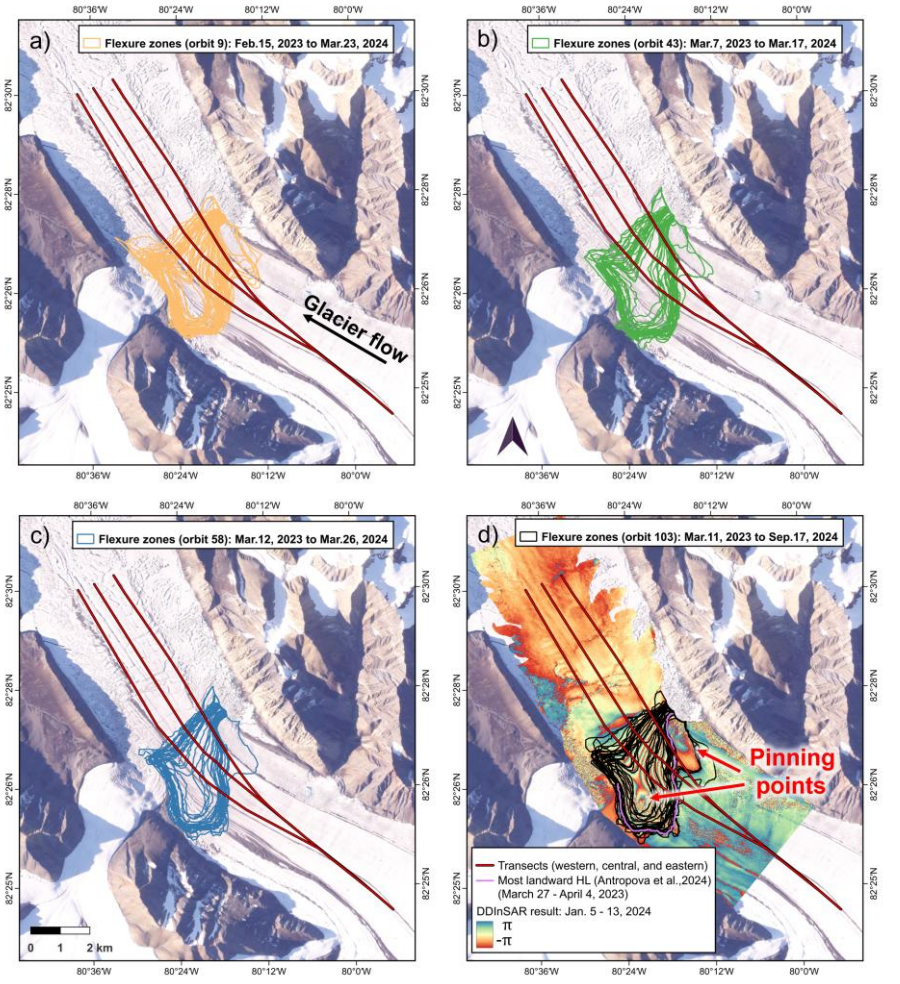
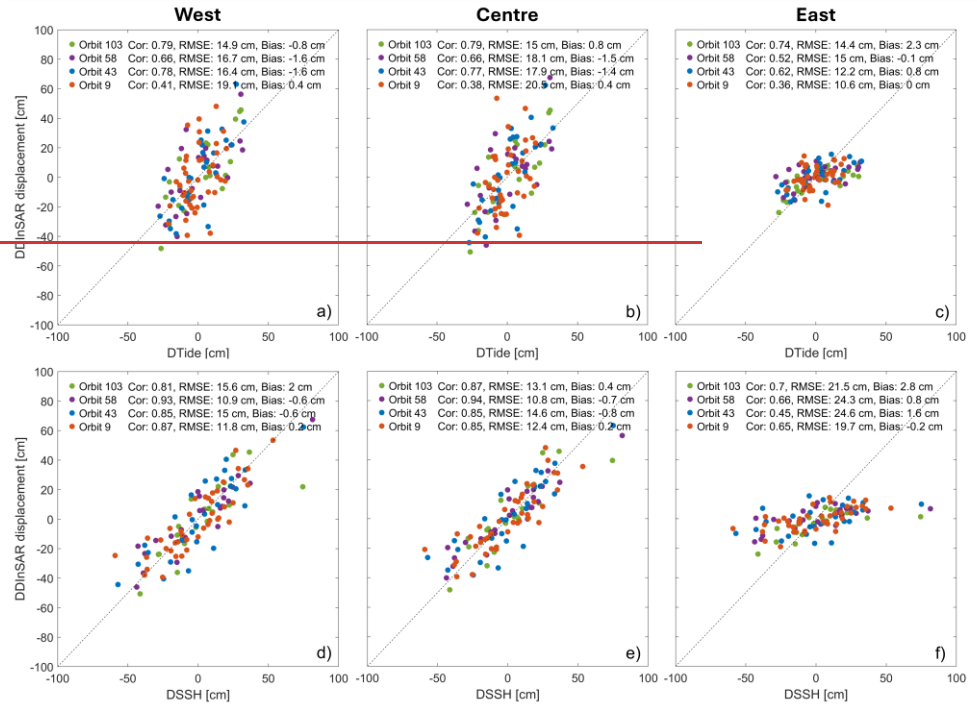


Figure 3: Flexure-zone**Z** delineations based on 2023-2024 RCM data acquisitions and overlayed on a Planet image acquired on August 12, 2024 (Image © [2024] Planet Labs PBC). a) Orbit 09 delineations: 42 orange polygons. b) Orbit 43 delineations: 27 green polygons. c) Orbit 58: 25 blue polygons. d) Orbit 103: 22 black polygons overlying a **D**DInSAR example that revealsshowing two pinning points on both sides of the glacier. A pronounced retreat associated with the formation of a new notch around the pinning

point (Fig. A2) at~~on~~ the eastern margin was discovered in October 2023, after the March-April 2023 hinge line delineations ~~in 2023~~ by Antropova et al. (2024).

3.2 Tidal analysis and ice-surface height reconstruction results

In~~For~~ Milne Fiord, the T_TIDE-simulated tidal range spanned from –20 cm to 21 cm over the observation period. After ~~correcting~~adding ~~for~~ IBE, the range increased 2.3-fold, spanning from –44 cm to 50 cm. T_TIDE-simulated tides that were IBE-corrected with in situ atmospheric pressure (i.e., displacement of sea surface height, DSSH) had a higher correlation with DInSAR-derived displacement (Fig. 4) than uncorrected simulated tides (Fig. A3 a-c) or simulated tides with GEM-based IBE-correction (Fig. A3 d-f). ~~This change of tidal range resulted in improved correlation with the DDInSAR-derived displacement. We found that sea surface displacement caused by tides alone (DTide in Fig. 4 a, b, c) had lower correlation with DDInSAR-derived displacement than sea surface displacement caused by both, tides and atmospheric pressure (DSSH in Fig. 4 d, e, f). This is most evident along T~~the western and central transects showed~~, where the~~ correlation coefficients (r) between DInSAR-derived displacement and DSSH ranging~~e of 0.38 – 0.79 increased to~~ from 0.81 to~~ –~~ 0.94~~, when the IBE was included. In general, both~~ RMSE values of 10.8 to 15.7 cm, and biases of -0.8 to 2 cm~~. and bias were also lower when atmospheric pressure was accounted for~~. The eastern side was not as well correlated (correlation coefficients ranging from 0.45 to 0.70, RMSE values of 20.0 to 24.6 cm, and biases of -0.2 to 2.9 cm), as ~~since~~ it was mostly grounded throughout the study period, yielding ~~a~~ very small ~~D~~DInSAR-derived surface displacements. ~~These correlation results corroborate the hypothesis that tides, along with atmospheric pressure, govern grounding line migration of Milne Glacier. They also highlight the importance of atmospheric pressure in controlling grounding line dynamics in fjords with relatively small tidal ranges. For Milne Fiord, the simulated tidal range spanned from –20 cm to 21 cm over the observation period. After correcting for IBE, the range increased 2.3-fold, spanning from –44 cm to 50 cm. This change of tidal range resulted in improved correlation with the DDInSAR-derived displacement.~~


West
Centre
East
Orbit 103 Cor: 0.79, RMSE: 14.9 cm, Bias: -0.8 cm
Orbit 58 Cor: 0.66, RMSE: 16.7 cm, Bias: -1.6 cm
Orbit 43 Cor: 0.78, RMSE: 16.4 cm, Bias: -1.6 cm
Orbit 9 Cor: 0.41, RMSE: 19.1 cm, Bias: 0.4 cm
Orbit 103 Cor: 0.79, RMSE: 15 cm, Bias: 0.8 cm
Orbit 58 Cor: 0.66, RMSE: 18.1 cm, Bias: -1.5 cm
Orbit 43 Cor: 0.77, RMSE: 17.9 cm, Bias: -1.4 cm
Orbit 9 Cor: 0.38, RMSE: 20.9 cm, Bias: 0.4 cm
Orbit 103 Cor: 0.74, RMSE: 14.4 cm, Bias: 2.3 cm
Orbit 58 Cor: 0.52, RMSE: 15 cm, Bias: -0.1 cm
Orbit 43 Cor: 0.62, RMSE: 12.2 cm, Bias: 0.8 cm
Orbit 9 Cor: 0.36, RMSE: 10.6 cm, Bias: 0 cm
DDInSAR displacement [cm]
DTide [cm]
a)
b)
c)
Orbit 103 Cor: 0.81, RMSE: 15.6 cm, Bias: 2 cm
Orbit 58 Cor: 0.93, RMSE: 10.9 cm, Bias: -0.6 cm
Orbit 43 Cor: 0.85, RMSE: 15 cm, Bias: -0.6 cm
Orbit 9 Cor: 0.87, RMSE: 11.8 cm, Bias: 0.2 cm
Orbit 103 Cor: 0.87, RMSE: 13.1 cm, Bias: 0.4 cm
Orbit 58 Cor: 0.94, RMSE: 10.8 cm, Bias: -0.7 cm
Orbit 43 Cor: 0.85, RMSE: 14.6 cm, Bias: -0.8 cm
Orbit 9 Cor: 0.85, RMSE: 12.4 cm, Bias: 0.2 cm
Orbit 103 Cor: 0.7, RMSE: 21.5 cm, Bias: 2.8 cm
Orbit 58 Cor: 0.66, RMSE: 24.3 cm, Bias: 0.8 cm
Orbit 43 Cor: 0.45, RMSE: 24.6 cm, Bias: 1.6 cm
Orbit 9 Cor: 0.65, RMSE: 19.7 cm, Bias: -0.2 cm
DDInSAR displacement [cm]
DSSH [cm]
d)
e)
f)

505

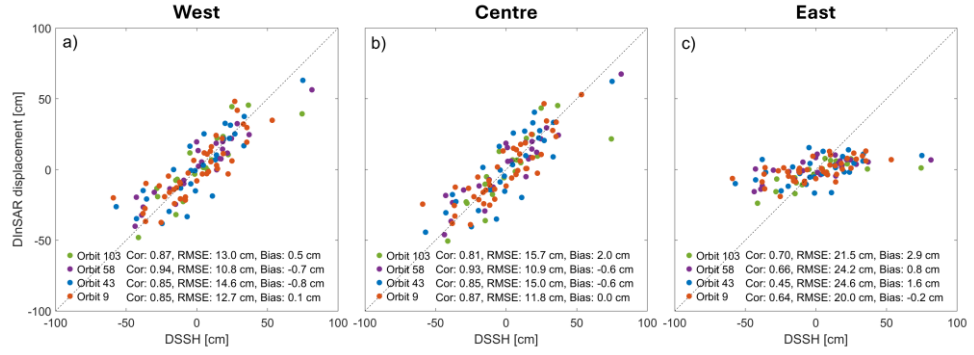
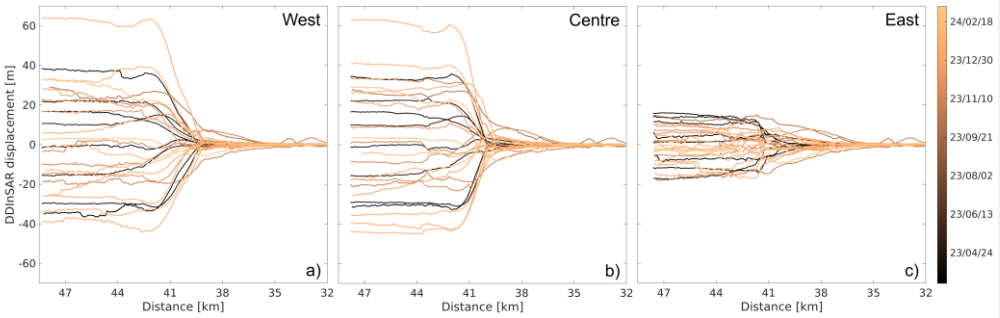

West
Centre
East
a)
b)
c)
Orbit 103 Cor: 0.87, RMSE: 13.0 cm, Bias: 0.5 cm
Orbit 58 Cor: 0.94, RMSE: 10.8 cm, Bias: -0.7 cm
Orbit 43 Cor: 0.85, RMSE: 14.6 cm, Bias: -0.8 cm
Orbit 9 Cor: 0.85, RMSE: 12.7 cm, Bias: 0.1 cm
Orbit 103 Cor: 0.81, RMSE: 15.7 cm, Bias: 2.0 cm
Orbit 58 Cor: 0.93, RMSE: 10.9 cm, Bias: -0.6 cm
Orbit 43 Cor: 0.85, RMSE: 15.0 cm, Bias: -0.6 cm
Orbit 9 Cor: 0.87, RMSE: 11.8 cm, Bias: 0.0 cm
Orbit 103 Cor: 0.70, RMSE: 21.5 cm, Bias: 2.9 cm
Orbit 58 Cor: 0.66, RMSE: 24.2 cm, Bias: 0.8 cm
Orbit 43 Cor: 0.45, RMSE: 24.6 cm, Bias: 1.6 cm
Orbit 9 Cor: 0.64, RMSE: 20.0 cm, Bias: -0.2 cm
DInSAR displacement [cm]
DSSH [cm]

Figure 4: ~~**Correlation results calculated for the three transects. Upper panels: correlation between DDInSAR displacement and displacement of simulated tides (DTide) for the: a) western, b) central, and c) eastern transects. Lower panels: C**~~**correlation between** ~~**D**~~**DInSAR displacement and displacement of sea surface height (DSSH) for the: d) western, e) central, and f) eastern transects. The different orbits are denoted by coloured symbols. 'Cor' - the Pearson correlation coefficient, 'RMSE' - Root mean square error, the 1:1 is plotted as a dashed line.**

~~Unwrapped and corrected~~ ~~S~~surface displacement of the floating ice tongue, calculated from unwrapped DInSAR imagery corrected for phase jumps, varied between -40 cm and 60 cm along both western and central transects (Fig. 5 a, b), but this variation was smaller (between -20 cm and 20 cm) along the eastern transect (Fig. 5 c). This also implies that~~T~~hus, most of the time, the eastern part of the glacier ice was grounded with negligible ~~D~~DInSAR displacement. ~~-~~The shape of the surface displacement curves suggests that ice ungrounding mostly occurs between 38 and 40 km downglacier from point A. Two prominent surface displacement bumps, approximately 3 cm in height, located between 32 and 35 km[DM1.1], were derived from DInSAR images based on SAR acquisitions with relatively large temporal gaps. Specifically, the first DInSAR image was generated from RCM data acquired on September 15 (SSH: −8.3 cm), September 19 (SSH: −7.9 cm), October 17 (SSH: 4.4 cm), and October 21 (SSH: 9.8 cm) 2023. The second DInSAR image was computed from acquisitions on October 21 (SSH: 9.8 cm), October 25 (SSH: 13.8 cm), November 2 (SSH: −8.6 cm), and November 6 (SSH: 6.3 cm) 2023. Our uncertainty analysis, discussed in detail below, confirmed that errors due to ice bending were low, whereas velocity-related errors exceeded the steady-period mean value for both DInSAR images. Therefore, we attribute these bumps to velocity variability and the associated surface changes occurring within the acquisition intervals.

Both curves also illustrate an additional noticeable displacement trend, diverging from zero at approximately 36 km and subsequently increasing or decreasing up to 7 cm. The same trend was observed in two other DInSAR images based on SAR acquisitions from: 1) November 6, 2023 (SSH: 6.4 cm), November 10, 2023 (SSH: 4.9 cm), and November 14, 2023 (SSH: −0.8 cm); and 2) March 1, 2024 (SSH: 4.5 cm), March 5, 2024 (SSH: 19.4 cm), February 10, 2024 (SSH: −3.3 cm), and February 14, 2024 (SSH: −12.1 cm). Errors due to velocity variability and ice bending were small (only a bending error of 0.1 cm in the March–February DInSAR image exceeded the mean error value) and well below the observed displacement. We attribute this displacement pattern to the combined effect of low and high tides, which likely induced a viscoelastic ice response (Wild et al., 2018).

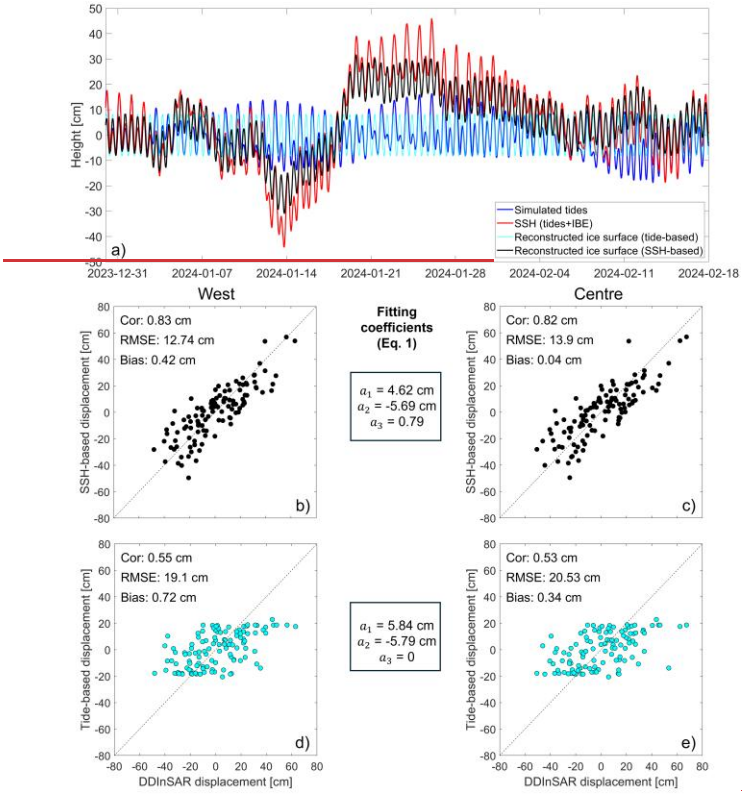


535 **Figure 5: An example of ~~D~~DInSAR-derived surface displacement from orbit 43 along the: a) western, b) central, and c) eastern transects starting at km 32 of the 2014 IceBridge radar profile (i.e., point A in Fig. 1). The line-of-sight errors due to tidal bending and velocity variability for orbit 43 are relatively low (Figure 7 c, d). During the steady period, the combined line-of-sight mean error is 0.12 cm, whereas during the unsteady period it is 0.3 cm. These errors result in uncertainties of ±7.4 m (i.e., less than one pixel) and ±18.4 m (i.e., less than two pixels), respectively, for the hinge-line delineations.**

Formatted: Not Highlight

Formatted: Not Highlight

540 ~~The ice surface height time series, reconstructed using the dominant tidal constituent M2 and DDInSAR displacement (Fig. 6 a), highlights the importance of IBE in DSSH calculations. SSH-based reconstruction (Fig. 6 b, c) resulted in a much better agreement with the computed DDInSAR displacement than tide-based reconstruction (Fig. 6 d, e) indicating higher correlation, lower RMSE and bias, respectively.~~



545 ~~Figure 6: Reconstructed ice surface height. a) Time-series of ice surface heights, tides, and sea surface heights (SSH, i.e., tides corrected for the inverse barometer effect, IBE). Correlation results for reconstructed displacement and DDInSAR-based displacement calculated for the tide-based reconstruction along the: b) western and c) central transects, and for SSH-based reconstruction along the: d) western and e) central transects. Number of observations, N: 114.~~

Our hypothesis that the newly observed notch formed during periods of high SSH, leading to seawater intrusion and ice
550 ungrounding around the eastern pinning point, was evaluated using s~~S~~tatistical characteristics of SSH (i.e., sea surface heights at the time of SAR data acquisitions rather than their displacement values of DSSH) along the eastern transect. The calculated characteristics for the ~~D~~DInSAR results were divided into two groups 1) cases without the notch, and 2~~1~~) cases when the notch was observed~~, are shown in~~ (Table 3). Average minimum SSH conditions were similar (-0.09 m vs. -0.08 m) for both groups

Formatted: Normal

of our results, which was also confirmed by the two-sample t-test with high p-value of 0.8. The average maximum SSH was higher for observations associated with the notch presence (0.21 m vs. 0.13 m for observations with and without a notch, respectively). A two-sample t-test resulted in a low p-value of 0.009, confirming the statistical significance of this difference. The standard deviation was also higher for observations with the notch, than without (0.13 m vs. 0.10 m) since this group was associated with higher maximum SSH values. These results~~us~~ support the interpretation that~~, with~~ higher SSH allows~~,~~ seawater ~~likely~~ to intrude~~s~~ f~~a~~urther inland, leading to ~~causing~~ the observed notch. ~~a larger FZ and GZ span.~~ The associated ~~i~~Ice displacement and localized flexure around the eastern pinning point creates the ~~a "bull's~~characteristic "bull's-eye" pattern in our ~~D~~DInSAR ~~results~~images.

Table 3. SSH statistical characteristics for the eastern transect.

Values averaged across all ~~D~~DInSAR observations	Notch observed	No notch observed
Standard deviation (m)	0.13	0.10
Minimum SSH (m)	-0.09	-0.08
Maximum SSH (m)	0.21	0.13

The ice-surface height time series, reconstructed using a regularized least-squares approach based on 59 tidal constituents and DInSAR displacement, is shown in Fig. 6. The differential reconstructed ice surface displacement and DInSAR displacement are highly correlated (r= 0.97) and yield an RMSE of approximately 5 cm for both the western and central transects during the steady period, which is reasonable given that our SSH showed a correlation of 0.96 and an RMSE of 3.4 cm with in situ tidal observations (Fig. A1).

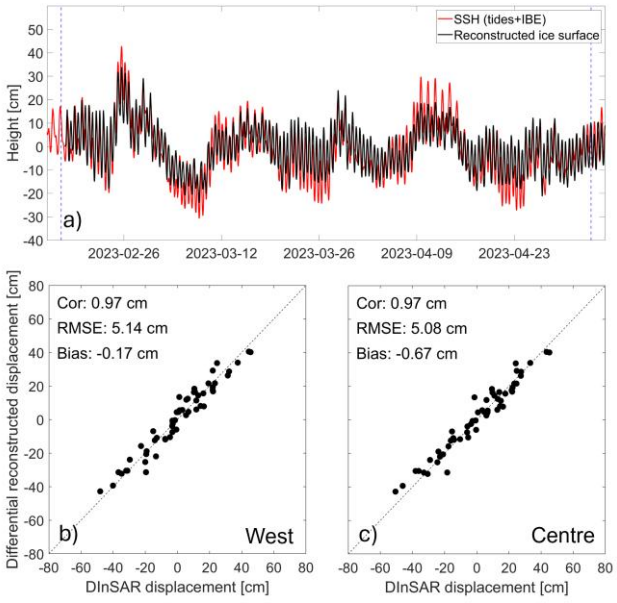


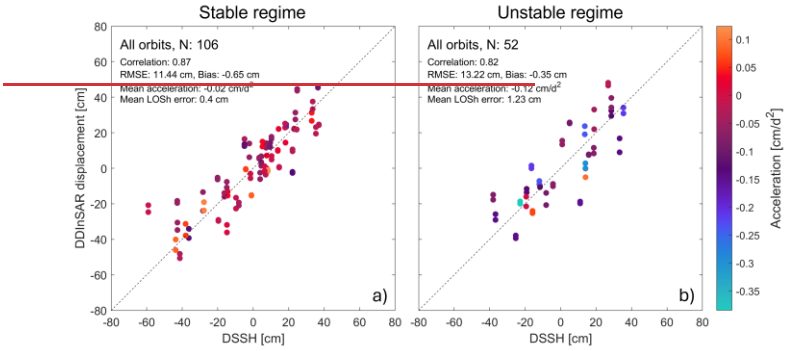
Figure 6: Reconstructed ice surface height. a) Time-series of ice surface heights and sea surface heights (SSH, i.e., tides and the inverse barometer effect, IBE). Relationship between the differential reconstructed displacement and DInSAR-based displacement calculated along the: b) western and c) central transects. Number of observations is 55.

3.3 Uncertainty analysis results

~~The~~ Our results indicate differences between ~~stable~~ steady and ~~unstable~~ unsteady glacier velocity ~~regimes~~ periods along both~~,~~ the western and central transects ~~for~~ in all four orbits (Fig. 4A). The steady period had lower mean deceleration (0.02 cm/d^2 vs. 0.12 cm/d^2) and higher DSSH vs DInSAR-derived displacement correlation (0.87 vs. 0.82) relative to the unsteady period. ~~is presented in Fig. 7. We found that the stable regime was associated with lower mean absolute acceleration (0.02 cm/d^2 vs. 0.12 cm/d^2) than unstable regime, which, in turn, resulted in a lower mean LOSh error (0.4 cm for the stable vs. 1.23 cm for the unstable regimes). In addition, these results were associated with higher correlation between DSSH and DDInSAR displacement (of 0.87 and 0.82) and~~ The resulting error due to velocity variability (LOShV) is threefold higher during the unsteady period than during the steady period (1.23 cm vs. 0.4 cm). Moreover, the error due to ice bending (LOShB) is also higher during the unsteady period relative to the steady period (0.52 cm vs. 0.37 cm along the central transect and 0.54 cm vs.

Formatted: Centered

0.38 cm along the western transect). ~~lower RMSE (11.44 cm vs. 13.22 cm) in the stable rather than in the unstable regime, respectively.~~

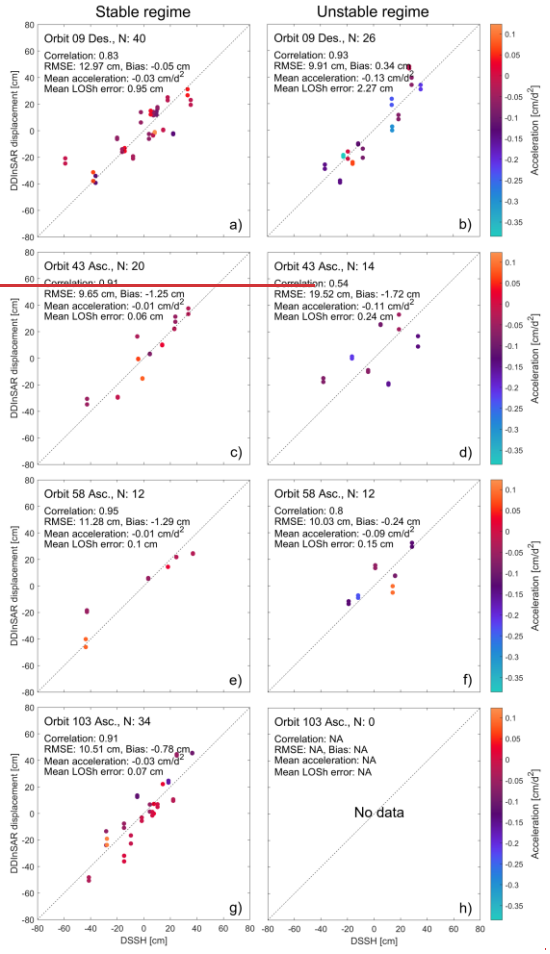


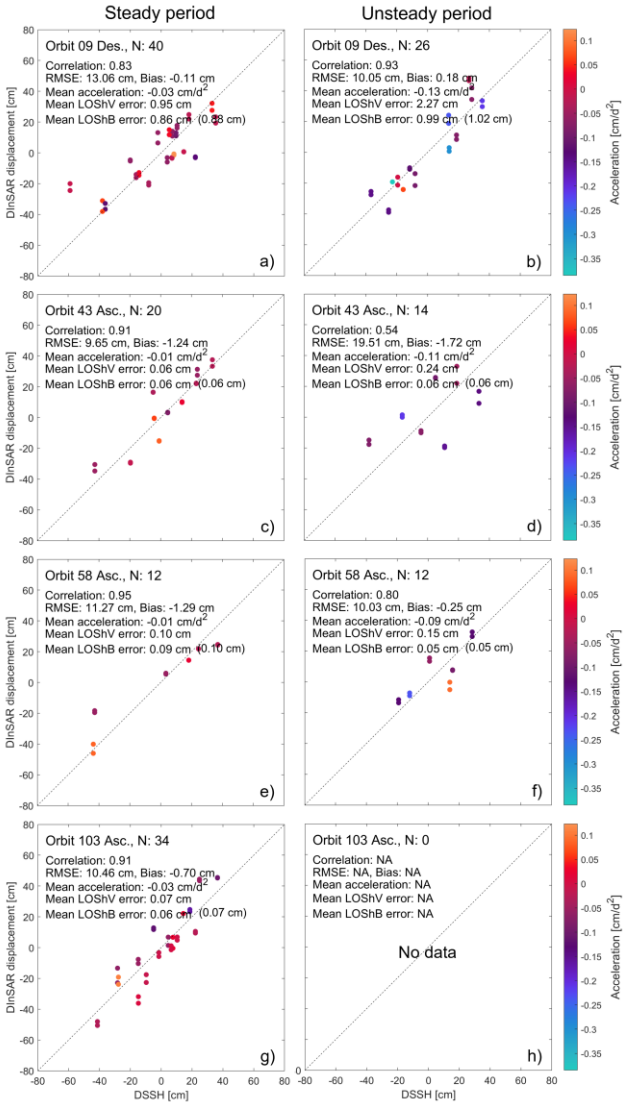
~~Figure 7: DDInSAR-derived displacements versus DSSH combined along the western and central transects with respect to the two glacier velocity regimes. a) Stable regime with minimal changes in velocities and b) unstable regime with more pronounced changes in velocities as defined in Fig. 2.~~

These results are more informative when examined with respect to each of the four orbits, as the sensitivity of DInSAR measurements to vertical and horizontal motion components depends on the incidence angle and look geometry (e.g., Rocca et al., 2010; Hu et al., 2014). ~~When these~~The correlation ~~-~~between DSSH and DInSAR-derived displacement, ~~results~~ mean LOShV error, and mean LOShB error ~~were analysed by orbit~~ for steady and unsteady periods in each of the four orbits are shown in ~~(~~Fig. 7~~8~~).~~,~~ W~~w~~e again found that mean absolute d~~ea~~celeration and mean LOShV error values were consistently lower for the ~~stable regime~~steady period than for the ~~unstable~~ unsteady one for all four orbits. The mean LOShB errors were low (0.05 cm – 0.10 cm) for ascending orbits with low incidence angles (i.e., orbits 43, 58, and 103) but were relatively high (0.86 cm – 1.02 cm) for the descending orbit with high incidence angle (i.e., orbit 09) during both periods.

The ascending orbits with low incidence angles ~~(i.e., orbits 43, 58, and 103)~~ showed high correlation between DSSH and ~~D~~DInSAR displacement (0.91 – 0.95 in Fig.7 c, e, g) for the ~~stable regime~~steady period, which was higher than correlation shown for the ~~unstable regime~~unsteady period (0.54 – 0.8~~0~~ in Fig. 7~~8~~ d, f). RCM orbit 43 results were associated with 11 times higher deceleration during the ~~unstable~~ unsteady than ~~stable~~ the steady ~~regime~~ period (-0.11 cm/d^2 vs. 0.01 cm/d^2~~-~~), which resulted a 4-fold increase in LOShV error (0.06 cm vs. 0.24 cm) and~~in~~ the lowest observed correlation (0.54) between DSSH and ~~D~~DInSAR displacement. This example underscores that pronounced changes in velocity violate the DInSAR assumption of invariant velocities between SAR data acquisitions and reduce the correlation between DSSH and DInSAR displacement. Therefore, the DInSAR images should be interpreted with consideration of errors arising from variable velocity. Descending orbit 09, with a high incidence angle, exhibited the opposite pattern: a higher correlation during the ~~unstable~~ unsteady period

than during the steady~~stable~~ period (0.93 vs. 0.83 in Fig.~~7~~8 a, b) ~~regime~~, which we attribute to its higher sensitivity to horizontal displacement and, consequently to velocity variability as well as ice extension and compression due to tidal bending.~~,~~ The largest mean LOShB error (0.99 cm) for orbit 09 resulted from its more frequent high-tide observations compared to the other orbits during the unsteady period.





Formatted: English (Canada)

Figure 78: ~~D~~DInSAR-derived vertical displacements versus differential sea surface height (DSSH) along the western and central transects with respect to the glacier velocity ~~regimes~~ periods as defined in Fig. 2. ~~Stable~~ Steady ~~regime~~ period with minimal changes in velocities ~~for four obits~~ and low line-of-sight ~~LOSh~~ errors for four orbits: a), c), e), g); and ~~unstable~~ unsteady ~~regime~~ period with more pronounced changes in velocities and high line-of-sight ~~LOSh~~ errors for four orbits: b), d), f), h). LOShV represents error due to variable velocity based on in situ GNSS records, and LOShB represents error due to ice surface extension or compression from tidal bending along the central (western) transect.

Formatted: Normal

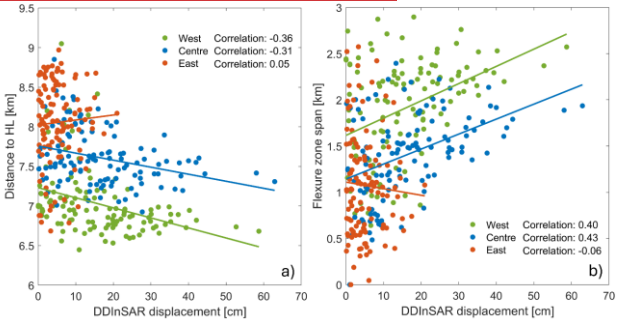
~~Our analysis indicates that changing glacier velocities contributed a minor LOSh error to our DDInSAR results (< 1cm for all observations, except for orbit 09 with a LOSh of 2.27 cm during the unstable regime) for DSSH ranging from –59 cm to 81 cm during our observations, confirming the robustness of the DDInSAR method during both regimes~~. The three ascending orbits with low incidence angles yielded the most reliable results, characterized by high correlations between DSSH and DInSAR-derived displacements and the lowest mean LOShV and LOShB errors during the steady period. In contrast, descending orbit 09, acquired at a high incidence angle, exhibited the highest mean LOShV and LOShB errors during the unsteady period. Along the central transect during the steady period, the combined mean LOShV and LOShB errors for orbits 43 and 103 were 0.12 cm and 0.13 cm, respectively. These combined line-of-sight errors represented 4.4% and 4.7% of the vertical displacement detected within a single RCM DInSAR fringe for orbits 43 and 103, respectively. Given the calculated median horizontal fringe width of 168.7 m (mean: 236.5 m; modal bin range: 100–120 m, representing 15% of total observations), the corresponding horizontal uncertainty during the steady period was approximately ±7–8 m, which is less than one pixel.

During the unsteady period for orbit 09, the maximum combined line-of-sight error along the central transect was 3.26 cm. Given the median horizontal fringe width of 187.1 m (mean: 212.5 m; modal bin range: 160–180 m, representing 16% of total observations), this corresponds to a horizontal uncertainty of ±221.8 m (i.e., approximately 22 pixels) for the flexure-zone delineations. Thus, flexure-zone delineations from orbits 43 and 103 during the steady period represent the most reliable results, with the lowest uncertainty, whereas delineations from orbit 09 during the unsteady period exhibit the greatest uncertainty.~~Ascending orbits with low incidence angle yielded the most reliable results with the lowest LOSh and high correlation during the stable season, while descending orbit 43 with high incidence angle had the highest LOSh. Nevertheless, orbit 43 demonstrated higher correlation between DDInSAR-derived displacements and DSSH for unstable than stable regime, which we attribute to a different viewing geometry.~~

3.4 Grounding-line migration and grounding-zone width results

~~The idea that the largest absolute tides are likely associated with the most pronounced grounding line migration inland and the largest span of FZ was examined through the association between DDInSAR surface displacement and FZ variables shown in Fig. 9 for the western, central, and eastern transects. Our results showed that the distance from point A to the hinge line, indeed, had a small tendency to decrease with increasing absolute DDInSAR displacement as there was a modest correlation of –0.36~~

~~and -0.31 between these variables in the western and central transects (Fig. 9 a). The FZ span tends to be larger with increasing absolute DDInSAR displacement (correlation of 0.40 and 0.43 for the western and central transects, respectively; Fig. 9b). The eastern transect did not show any association between the analysed FZ variables and absolute DDInSAR displacement because this part of the glacier was predominantly grounded as indicated by the minor surface displacements (Fig. 5 c) and the most pronounced changes in the FZ were associated with the sea water intrusions around the eastern pinning point. The difference in the correlation between the western and central transect can likely be attributed to the presence of the pinning point near the western margin. Pinning points serve as physical anchors that support the floating ice tongue and, thus, affect the distance at which the hydrostatic equilibrium is reached with changing tides as well as how far inland water can intrude with changing tides. The bed topography that enhances water intrusions, therefore, plays an important role in shaping the FZ and positioning the grounding line.~~



~~**Figure 9: Association between DDInSAR surface displacement and FZ variables along the western, central, and eastern transect. a) Distance from Point A to hinge line (HL) and DDInSAR-derived surface displacement overlayed by lines of linear best fit. b) FZ span along the three transects with respect to DDInSAR surface displacement overlayed by lines of linear best fit.**~~

The maximum and minimum distances from point A to the hinge line derived from all orbits are shown in Table 4, and the associated RCM SAR data acquisitions and SSH are presented in Fig. 9. The resulting grounding zone widths derived from these distances are generally larger for the western and eastern transects than for the central transect for all orbits, except for orbit 43. The largest grounding zone widths along the three transects are associated with orbit 103, which has low uncertainty (±8 m) during the stable period. In most cases (7 out of 12, highlighted in bold in Table 4), the standard deviation of SSH at the times of SAR acquisitions is higher for the minimum distance to the hinge line (i.e., the most landward hinge line position) than for the maximum distance (i.e., the most seaward hinge line position). Thus, the most landward hinge line positions are more often associated with larger SSH differences at the times of SAR acquisitions (Fig. 8).

Table 4. Results for the distances from point A to the hinge line, grounding-zone widths, and the associated SSH standard deviations.

Variables along the three transects	Relative orbit ID			
	09	43	58	103
Western transect:				
Distance: min – max (m)	6553 – 8414	6532 – 7352	6722 – 8208	6447 – 9048
Grounding zone width (m)	1861	820	1486	2601
SSH Standard deviation (cm) for min – max distances	**12.5 - 9.6**	10.3 - 13.4	9.7 - 9.8	8.5 - 10.1
Central transect:				
Distance: min – max (m)	7010 – 8379	7054 – 8256	7068 – 8364	6925 – 8850
Grounding zone width (m)	1369	1202	1296	1926
SSH Standard deviation (cm) for min – max distances	**13.2 - 9.6**	**10.3 - 7.3**	**29.8 - 9.8**	7.6 - 10.1
Eastern transect:				
Distance: min – max (m)	6786 – 8799	6999 – 8710	6880 – 8752	6684 – 8969
Grounding zone width (m)	2013	1710	1872	2285
SSH Standard deviation (cm) for min – max distances	**10.5 - 9.6**	**33.3 - 7.3**	**29.8 - 9.8**	7.6 - 10.1

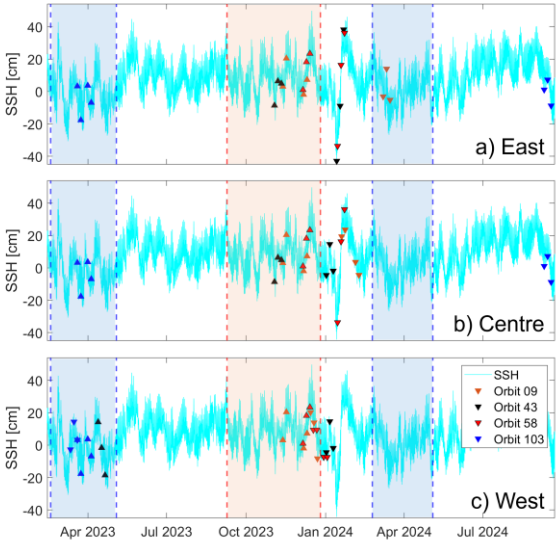


Figure 8: Timing of RCM SAR data acquisitions and the associated SSH values when the maximum (upward-pointing triangles) and minimum (downward-pointing triangles) distances from point A to the hinge line were detected in the DInSAR images resulting from these acquisitions along the (a) eastern, (b) central, and (c) western transects. The steady velocity period is highlighted in blue, and the unsteady period is highlighted in orange.

Formatted: Line spacing: single

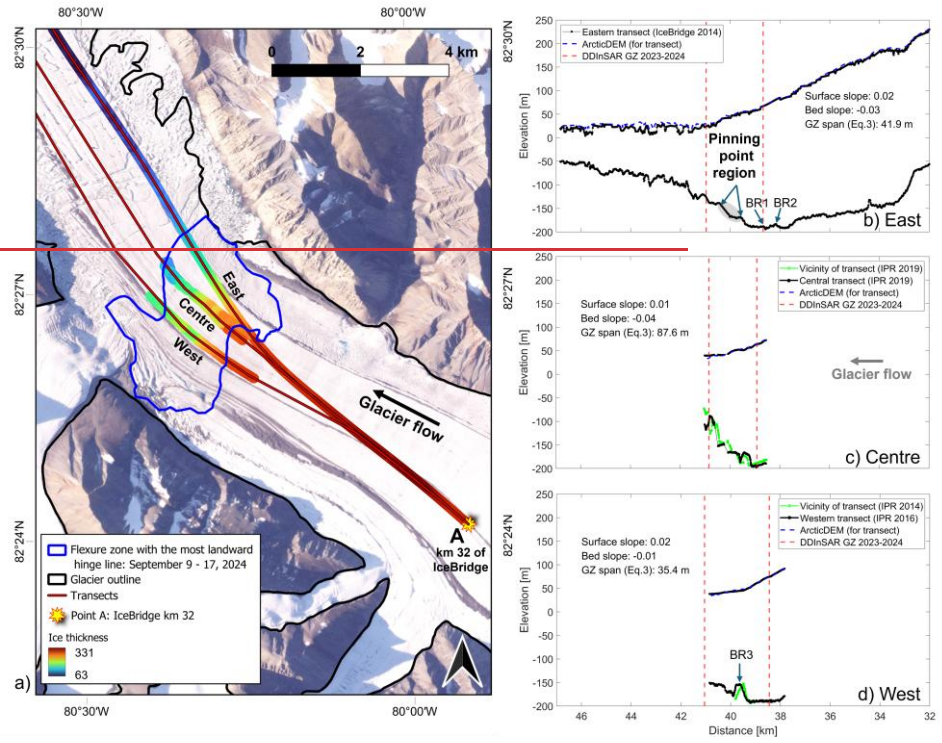
Formatted: Line spacing: single

Formatted: Line spacing: single

Formatted: Line spacing: single

Grounding zones derived from flexure-zone delineations during the steady period from orbits 43 and 103, which are characterized by the lowest uncertainty, as well as those for the entire study period, are shown in Fig. 9. ~~The DDInSAR-derived GZs shown with vertical red dashed lines in Fig. 10~~ The steady period grounding-zone width fully coincided with that of the entire study period for the western transect, and is smaller by 270 m and 306 m for central and eastern transects, respectively. The most landward grounding-zone limits for the entire study period along the central and eastern transects were based on orbit 103 RCM data acquisitions in September 9-17, 2024. Since this orbit is less sensitive to errors due to velocity variability and ice bending, this landward migration of the hinge line is likely due to post-summer melt changes rather than uncertainty; thus, we consider the grounding zone width over the entire study period to be reliable. ~~b-d~~

The Milne Glacier grounding zone ~~were all~~ is associated with retrograde bed slopes along the three transects. The ~~GZ span~~grounding-zone width over the entire study period was 2.3 km along the eastern, 1.9 km along the central and 2.6 km along the western transects (Fig. ~~10~~9), which was about 55, 22 and 74 times larger, respectively, than calculated from the hydrostatic equation (Eq. 3). The western transect (Fig. ~~10~~ 9 d), associated with the shallowest bed slope, had the largest ~~GZ span~~grounding-zone width, whereas ~~and~~ the central transect (Fig. 9~~10~~ c), associated with the steepest slope, had the smallest ~~GZ span~~grounding-zone width, which ~~is~~ aligne~~s~~d with the theory (Tsai & Gudmundsson, 2015) and ~~literature~~ observations from elsewhere (e.g., Rignot et al., 2024). ~~-~~In addition, our ~~D~~DInSAR ~~results~~ images suggest the presence of a pinning point farther westward of the bed rise ('BR3' in Fig. 9~~10~~ d) between km 38 and km 39 of the western transect. This likely further amplifies the effect of the shallow slope by bridging the ice to the area where the bathymetry becomes shallower up-glacier of the tributary glacier that merges with Milne Glacier. The eastern bed slope was also associated with the pinning point shown by our ~~D~~DInSAR ~~results~~images, which extended between the two bed rises at km 39.7 and km 40.7 highlighted ~~by~~ in grey ~~colour~~ in Fig. 9~~10~~ b. This pinning point altered the bed slope and the ~~span~~ width of the observed ~~GZ~~grounding zone, as~~. Additionally, the eastern pinning point~~it was linked to a pronounced retreat of the grounding line over the last portion of our SAR observation period, caused by seawater entering a cavity up-glacier of the pinning point. ~~The eastern transect bathymetry suggests that seawater intrusion further upglacier is likely currently inhibited by a small bed rise ('BR1' in Fig. 10 b) at km ~38.7 and could be later suppressed by a larger bed rise at km ~38.2 ('BR2' in Fig. 10 b), that will likely become the next landward position for the grounding line. Subsequently, another cavity on a retrograde slope may cause a rapid retreat of the grounding line down to km 37.5, where the bed slope changes to a prograde slope, which should slow down the grounding line's recession.~~


80°30'W
80°00'W
82°30'N
82°27'N
82°24'N
0
2
4 km
East
Centre
West
Glacier flow
A
km 32 of IceBridge
Flexure zone with the most landward hinge line: September 9 - 17, 2024
Glacier outline
Transects
Point A: IceBridge km 32
Ice thickness
331
63
a)
Eastern transect (IceBridge 2014)
ArcticDEM (for transect)
DDInSAR GZ 2023-2024
Surface slope: 0.02
Bed slope: -0.03
GZ span (Eq.3): 41.9 m
Pinning point region
BR1
BR2
b) East
Vicinity of transect (IPR 2019)
Central transect (IPR 2019)
Surface slope: 0.01
Bed slope: -0.04
GZ span (Eq.3): 87.6 m
c) Centre
Vicinity of transect (IPR 2014)
Western transect (IPR 2016)
Surface slope: 0.02
Bed slope: -0.01
GZ span (Eq.3): 35.4 m
BR3
d) West
Elevation [m]
Distance [km]

705

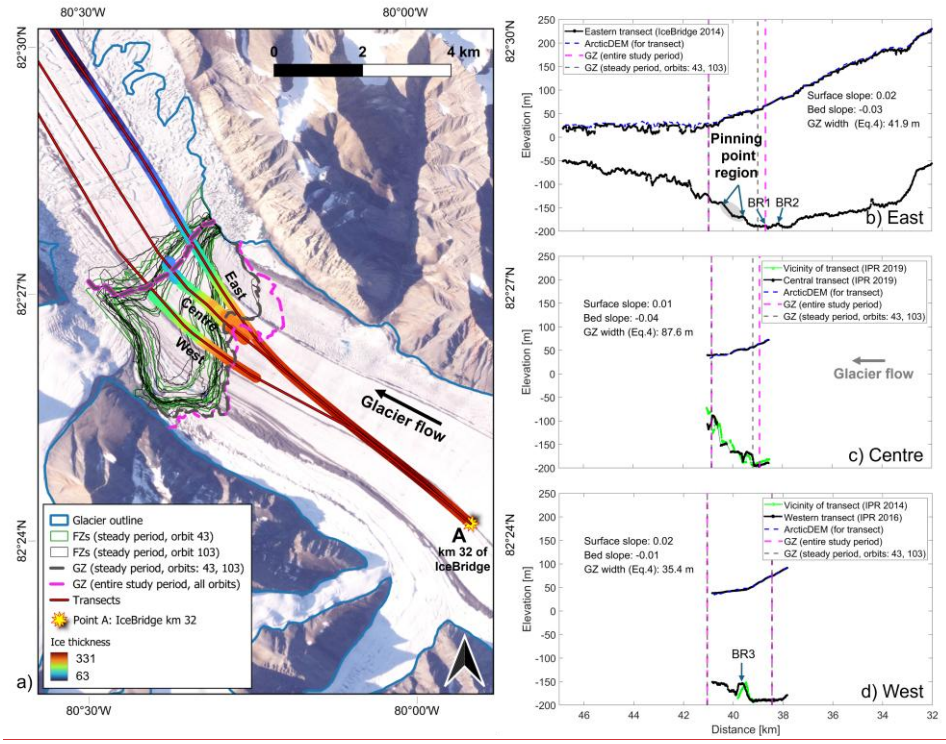
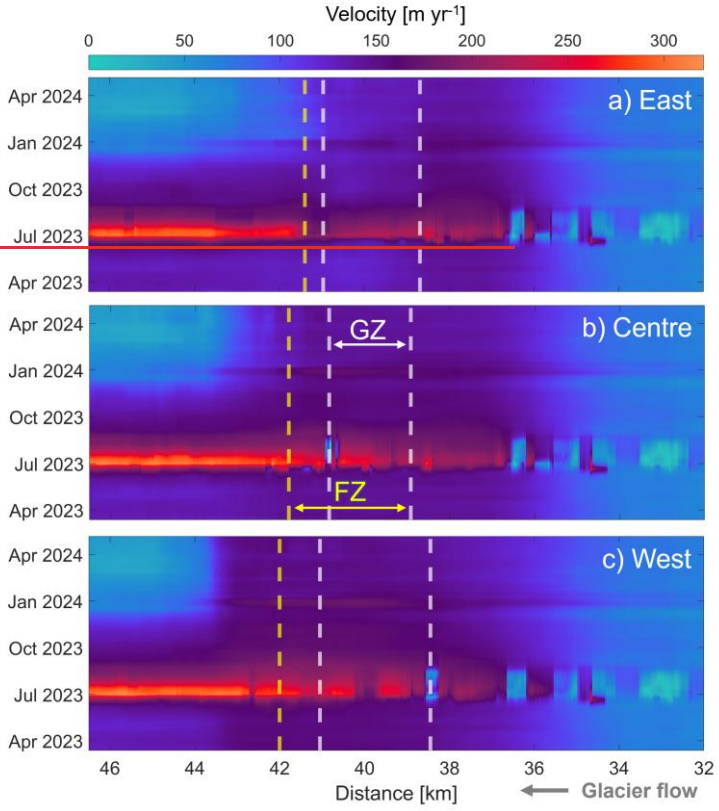


**Figure ~~9~~10: Retrograde bed and surface geometry of the Milne Glacier ~~near its GZ~~grounding zone. a) Grounding zones over the steady period (dark grey dashed lines) and the entire study period (magenta dashed lines). ~~The~~ The steady period grounding zone is based on the most ~~landward~~ reliable flexure-zone~~FZ boundaries~~ delineations (uncertainty of ±8 m) from orbits 43 (green) and 103 (black) ~~ed in September, 2024 (blue polygon)~~ overlaying the three transects and a Planet image from August 12, 2024 (Image © [2024] Planet Labs PBC). Surface and bed geometry retrieved from the IceBridge and field IPR ~~radar~~ observations and Arctic DEM along and in vicinity of b) eastern, ~~and~~ c) central, d) and western transects. The calculated width~~span~~ of the grounding zone~~GZ~~ (displayed in text) is about 22 to 74 times smaller than the ~~D~~DInSAR-derived grounding zone~~GZ~~, over entire study period. ~~(shown with red dashed lines).~~

Formatted: Normal

To provide context for the observed grounding-zone and flexure-zone widths with respect to changes in glacier velocities, and to allow direct comparison with previously reported annual velocities (Millan et al., 2017; Van Wychen et al., 2020), we present velocities in annual notation in Fig. 10. Over the period of our SAR observations, the Milne Glacier ~~FZ~~ flexure zone was associated with velocities of up to 270 m yr^{-1} during the summer (Fig. 1~~0~~1). The grounded ice moved downstream at about 100 m yr^{-1} and then accelerated to 200 m yr^{-1} at ~3 km up-glacier of the ~~FZ~~flexure zone, reaching a velocity of 270 m

yr^{-1} in the flexure zone~~FZ~~ and then up to 320 m yr^{-1} down-glacier of it during summer months. Hence, Milne Glacier ~~FZ~~ flexure zone was associated with up to ~2.7-fold increase of glacier velocity compared against its up-glacier grounded part shown in Fig. 10~~1~~.



Formatted: English (Canada)

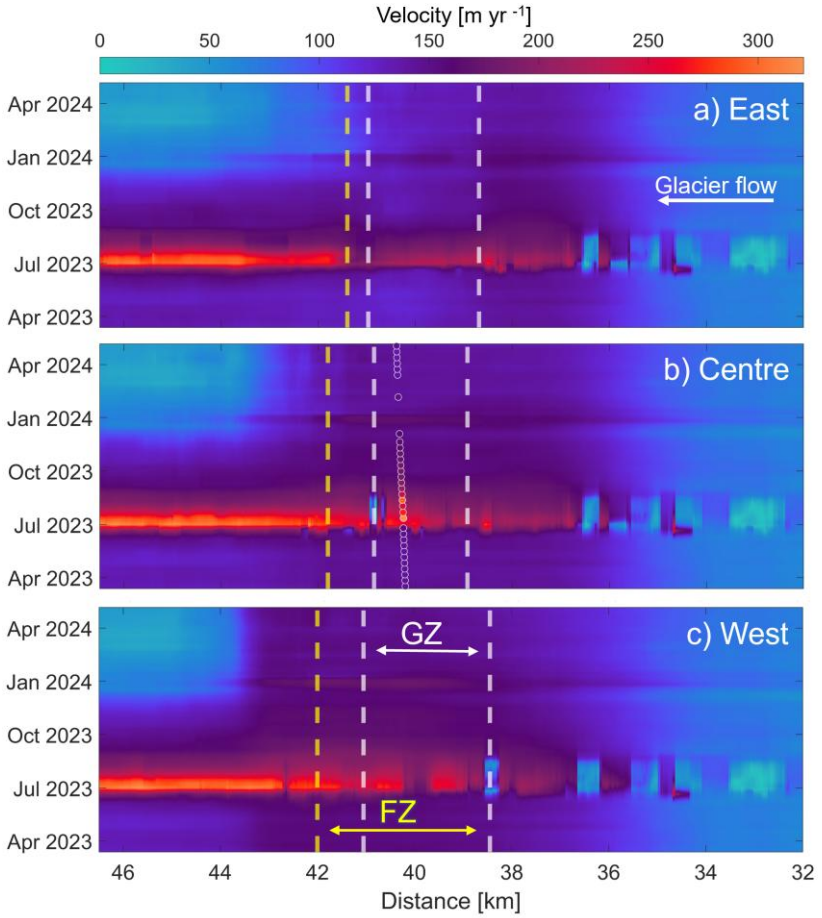


Figure 10~~1~~: Hovmöller diagram of SAR-derived Milne Glacier velocity along the a) eastern, b) central, and c) western transects with respect to ~~its~~ the grounding zone (GZ) and the largest ~~span~~ width of the flexure zone (FZ) marked by white and yellow dashed lines respectively over ~~period of~~the observation period~~s~~. The GNSS locations and associated velocities throughout the observation period are shown as a scatter plot overlaid on the SAR-derived velocities along the central transect. Profiles start at km 32 of the 2014 IceBridge radar transect. (point A in Fig. 1). Velocity fluctuations between km 32 and 37 in the summer are a noise-related artifact.

The grounding zone, where the grounding line migrated during the observation period, exhibited differences in velocity along the three transects. ~~The landward part of the FZ, associated with the GZ where the GZ migrated during the observation period, exhibited a pronounced shift in velocity, as this is the zone where ice flow becomes frictionless.~~ The ~~largest~~ widest ~~GZ~~ grounding zone ~~span~~ along the western transect of the glacier ~~(Fig. 11 a)~~ was associated with the highe~~st~~ velocity of 166.4 m yr^{-1}, averaged over a year and across the observed grounding zone width (Fig. 10 c), and the thickest ice (mean value of 225.6 m, Fig. 9 d). ~~,~~ This section discharge~~ding~~ approximately 37 540 m^3 yr^{-1} ~~more~~ of ice along a 1 m-wide flow line. ~~than~~ The narrower and thinner grounding zones along the ~~its central~~ eastern and ~~eastern~~ central transects, with (mean thicknesses of 210.0 m and 200.5 m ~~Fig. 11 b, c~~ (Fig. 9 b, c), were associated with slower average velocities of 144.6 m yr^{-1} and 159.8 m yr^{-1} (Fig. 10 a, b), discharged approximately 30 366 m^3 yr^{-1} and 32 040 m^3 yr^{-1} along a 1 m-wide flow line, respectively.

Formatted: Not Highlight

4. Discussion

~~This section summarizes our results and insights about the controls that drive short-term grounding line migration taking into account variations in glacier velocity and different SAR viewing geometry. Our observations also reveal patterns that contribute to long-term grounding line retreat.~~

4.1 Short-term migration of ~~GZ~~ grounding line and variability of flexure and grounding zones along the transects~~and FZ~~: SSH~~tides, atmospheric pressure,~~ and glacier geometry

The intra-annual ~~DDInSAR-derived~~ vertical displacement of the Milne Glacier ice tongue is governed by changes in ~~the~~ SSH, which, in turn, are driven by variations in tides and atmospheric pressure. ~~, While sea surface height (~~SSH~~)~~ has been identified as a major driving mechanism~~s~~ of grounding ~~-~~line migration for Thwaites Glacier in West Antarctica (Rignot et al., 2024), Fisher, Mellor, and Lambert glaciers in East Antarctica (Chen et al., 2023), and Jakobshavn Isbræ in Greenland (Kim et al., 2024. These locations have relatively large (i.e. ≥ 1 m) tidal ranges, therefore atmospheric pressure only plays a minor role in the displacement of floating ice shelves and ice tongues. ~~), our study highlights the important role atmospheric pressure can have in this process. Changes in atmospheric pressure result in an isostatic response of sea surface height (i.e., the inverse barometer effect), which then affects ice shelf surface elevation (Padman et al., 2003).~~ For marine-terminating glacier~~s~~ systems similar to Milne Glacier, where tidal range is much smaller than in the aforementioned studies, atmospheric pressure variability ~~has a pronounced effect~~ plays a more substantial role in controlling ~~on~~ SSH, and, consequently, ~~on~~ the displacement of the floating ice tongue. ~~observed from the DDInSAR results~~.

Based on the explored flexure-zone variables, such as distance to the hinge line and flexure-zone width, we found that the grounding line migrates differently with tides, forming distinctive flexure zones along the three transects due to variations in bed geometry, ice thickness, and likely ice stiffness. ~~Our findings~~ While the width of the flexure zone is governed by ice stiffness, which is determined by ice thickness and the effective Young's modulus (Wild et al., 2017), pinning points can

modify these relationships. Pinning points act to physically prop up the floating ice tongue, at least at certain water levels, thereby influencing local ice stiffness, ice flexure patterns, and the extent of inland water intrusion with changing tides. Previous studies have shown that the presence of pinning points affects lateral and basal shear stresses, generating upstream compression and downstream tension, which, in turn, influences flow variability and can locally enhance the stiffness of the glacier system (Robel et al., 2017; Still & Hulbe, 2021). In this study, both of the observed pinning points are located near the lateral shear zones, which are associated with reduced ice stiffness (Wild et al., 2025). Therefore, the complex interplay between local ice stiffness and glacier bed geometry results in the observed flexure-zone widths, which tend to be larger near the glacier margins where the pinning points are present.

Pinning points also control grounding-line migration and, consequently, the width of the grounding zone. Our results ~~corroborate~~support the idea that ~~shallow bed topography is associated with~~ a ~~larger span of~~ wider grounding zone is associated with shallow bed topography, whereas a narrower grounding zone is associated with steeper bed slopes ~~GZ~~ (Milillo et al., 2022; Rignot et al.,~~;~~ 2024) ~~than steep bed~~. The grounding line of Milne Glacier migrates along a retrograde bed slope over tidal cycles forming a distinctive ~~GZs~~ grounding zone along the three transects ~~with known geometry~~. The ~~largest GZ span~~widest grounding zone was observed along the shallowest western transect followed by ~~span over~~ eastern transect, and then over central transect with the steepest bed slope.

The overall bed slope in the ~~GZ~~ grounding zone helps to characterize its ~~span~~width, but local topography also plays an important role. For instance, Chen et al. (2023) used intervals associated with very distinctive bed features for their slope calculations (i.e., an interval within the Lambert Estuary's ~~GZ~~ grounding zone associated with retrograde slope and several intervals up-glacier of Fisher Glacier's ~~GZ~~ grounding zone associated with very steep prograde slopes) to demonstrate a quasi-exponential relationship between ~~GZ span~~grounding-zone width and bed slope. Milne Glacier's topography within its ~~GZ~~ grounding zone ~~associated with pinning points drastically~~ controlled ~~affected GZ~~ the grounding zone ~~span~~ width ~~along the eastern transect~~ over the period of observations: the newly detected notch, associated with a pinning point, caused a 30% increase in the grounding-zone width along the eastern transect ~~the grounding line migrated about 800 m upglacier (35% of the observed GZ span) when seawater intruded into a cavity upglacier of the pinning point~~. The grounding- line migration associated with the notch was even more extensive farther east, with landward incursion reaching up to 2.4 km further than the previous ~~GZ~~grounding zone. Thus, pinning points on retrograde slope ~~play an important role in grounding line migration and shaping GZ characteristics.~~

~~The relationships between DDInSAR vertical displacement and FZ variables such as distance to hinge line and FZ span were examined to explore patterns in the ice FZ with changes in SSH. Our results show that moderate linear relationships exist between DDInSAR displacement and distance to hinge line as well as FZ span. However, pinning points likely influence these relationships by serving as anchors for the floating ice tongue. The difference in the correlation between the western and central transect can likely be attributed to the presence of the pinning point near the western margin. Pinning points serve as physical anchors that support the floating ice tongue and, thus, affect the distance at which the hydrostatic equilibrium is reached with~~

~~changing tides as well as how far inland water can intrude with changing tides. The bed topography that enhances water intrusions, therefore, plays an important role in shaping the FZ and positioning the grounding line.~~

~~They~~ inhibit seawater intrusion into bed cavities during low SSH and permit water intrusions farther inland when SSH is high, thereby playing an important role in shaping the flexure zone and positioning the grounding line. Therefore, detailed information on bed geometry ~~in the GZ and farther~~ up-glacier of the grounding zone is essential for~~to~~ improving predictions ~~enhance our understanding~~ of grounding-line retreat, particularly for identifying where potential pinning points may form due to water intrusion and ice ungrounding around bed rises.~~and improve predictions of grounding line retreat~~.

4.2 Flexure zone delineation uncertainties ~~Migration~~ during ~~stable~~ steady and ~~unstable~~ unsteady velocity ~~regimes~~periods

This study is based on a commonly used DInSAR approach, which assumes steady glacier flow between SAR data acquisitions so that it can be isolated through interferogram differencing to reveal the vertical component of displacement due to tidal flexure. We examined the validity of this assumption by quantifying the SAR line-of-sight error caused by velocity variability using available in situ GNSS records. We also assessed SAR line-of-sight error resulting from ice extension and compression due to tidal bending. Analysis of these errors with respect to four RCM orbits with different incidence angles, and both ascending and descending passes - thus different sensitivities to horizontal flow variability - ~~Our analysis~~ provides insights about the robustness of our ~~D~~DInSAR flexure-zone delineations and the associated uncertainties. ~~derived results with respect to the RCM SAR viewing geometry and two velocity regimes, stable and unstable, defined based on in-situ velocity observations. The calculated mean LOSh errors were below 1 cm for both regimes and all orbits except for orbit 09 during the unstable regime, which yielded a mean LOSh of 2.27 cm.~~ We found that the RCM viewing geometry associated with low incidence angles (between 19º and 30º) and ascending tracks (i.e., orbits 43, 58 and 103) provided the most robust results for the Milne Glacier ~~FZ~~ flexure-zone delineation during the ~~stable~~ steady period ~~regime~~. Particularly, the most reliable flexure zone delineations with ± 8 m uncertainty and high correlation of 0.91 between DInSAR displacements and DSSH were attributed to orbits 43 and 103. The~~se~~ correlation results degraded with increasing changes in velocity, especially for orbit 43.~~, when the glacier decelerated by a factor of 11 (-0.01 cm/d² vs. -0.11 cm/d²) LOSh error increased 4-fold (0.06 cm vs. 0.24 cm)~~.

~~The descending RCM SAR pass (i.e., orbit 09) with a mean incidence angle of 39.6° had the highest mean LOSh error. However~~In contrast, the descending RCM SAR pass (i.e., orbit 09) with a mean incidence angle of 39.5° demonstrated high ~~the~~ correlation between ~~D~~DInSAR and DSSH ~~was high~~ during both, ~~stable~~ steady and ~~unstable~~ unsteady ~~regimes~~ periods (0.83 and 0.93, respectively) despite the highest mean LOShV and LOShV errors. This orbit was associated with the highest flexure zone delineation uncertainty of ±222 m resulting from the combined errors due to variable velocity and bending during the unsteady period. ~~We attribute this result to the different viewing geometry (i.e., descending path and high incidence angle),~~

~~which likely affected the correlation, as well as to the least well-defined distinction between the stable and unstable seasons among the considered orbits.~~ This uncertainty would increase if there was an even greater velocity variability. Additionally, larger tidal displacements and thicker ice can enhance errors associated with ice extension or compression caused by bending. For instance, the error due to ice bending can be on the order of one ice thickness based on a 1-D model (Rack et al., 2017). This effect can be inhibited within embayments and enhanced around protrusions of the grounding line, as suggested by a 2-D model (Wild et al., 2018). Thus, flexure-zone delineations from orbits with high incidence angles, which are sensitive to horizontal surface displacements, should be interpreted with consideration of the associated uncertainties when a glacier experiences velocity variability and/or pronounced tidal bending

~~The glacier decelerated only by a factor of ~4 (~0.03 cm/d² vs. ~0.13 cm/d²) and LOSh error increased 2-fold (0.95 cm vs. 2.27 cm).~~ Our investigation was limited by the number of ~~FZ~~ flexure-zone delineations during the ~~unstable season~~unsteady period due to relatively scarce summer SAR observations as well as lack of coherence during the summer season caused by both surface melt and acceleration of the glacier. With the increasing number of SAR observations, larger DInSAR datasets during the unsteady season can be used along with SAR-derived 2-D velocities (e.g., Samsonov et al., 2021), ~~along with reliable in-situ tidal and velocity observations, could help~~ to further investigate and quantify how the ~~grounding line and FZ~~ flexure-zone delineation is affected by the SAR viewing geometry with respect to changes in glacier velocity and ice bending across the entire glacier grounding zone.

~~4.3 Glacier FZ velocity~~

~~The glacier FZ plays a crucial role in ice dynamics, as it controls the discharge of ice from the grounded portion of the glacier (Schoof, 2007). The Milne Glacier's FZ and the rest of its floating ice tongue exhibited higher velocities than the grounded portion of the glacier, with velocities increasing by up to 2.7-fold as the glacier transitioned from grounded to floating in the summer. Moreover, the GZ with the largest span along the western transect showed higher velocities throughout our period of observations suggesting that a larger GZ span associated with a shallow bed geometry might promote increased ice flow into the ocean. The observed expansion of the GZ along the eastern transect might indicate future velocity increase in this part of the glacier. The computed average annual velocity varied from 170 to 195 m yr^{-1} in the FZ during the study period was similar to results for 1990s reported by Millan et al., (2017) and higher than observed velocities over recent years. Between 2010 and 2020, the glacier velocity in the FZ ranged from 80 to 160 m yr^{-1} with its maximum happening between 2018 and 2020 (Wychen et al., 2020). This study documented glacier acceleration, which was preceded by grounding line retreat, suggesting that the glacier is prone to dynamic thinning that could trigger further grounding line retreat. The newly observed notch in the eastern part of the glacier might suggest future changes in the glacier dynamics.~~

4.34 Long term grounding-line retreat and bed geometry

The Milne Glacier retrograde bed configuration in the ~~GZ~~ grounding zone allows ocean water to intrude landward with high tides behind two pinning points in its western and eastern margins. This~~and,~~ likely enhances ice deterioration far under the glacier ~~in this zone~~ which would promote grounding-line retreat. For instance, Poinelli et al. (2023) suggested that enhanced melt rates around pinning points can lead to the mechanical instability of an ice shelf/tongue. The observed rapid grounding-line retreat in the eastern part of Milne Glacier illustrates the combined effect of bathymetry and ocean forcing. Between 2011 and October of 2023, this part of Milne Glacier was stable and had much ~~smaller span of the GZ~~narrower grounding zone than western and central parts (Antropova et al., 2024). The eastern ~~GZ~~ grounding zone was also associated with a bed rise on a retrograde slope (before km 41 in Fig. 10 b), which, likely, inhibited the seawater intrusion further inland. As a result of melt processes during summer 2023, the grounding line migrated past the next inland bed rise shown as the landward bound of pinning point region in Fig. 10 b, and the new eastern landward limit of the ~~FZ~~ flexure zone was observed up to 2.4 km up-glacier at 'BR1' in Fig. 10 b. This suggests rapid changes as soon as seawater was able to intrude past the first bed rise, likely driven by the retrograde slope and permanently opened ocean cavities. The eastern transect bathymetry suggests that seawater intrusion further up-glacier is likely currently inhibited by a small bed rise ('BR1' in Fig. 10 b) at km ~38.7 and could be later suppressed by a larger bed rise at km ~38.2 ('BR2' in Fig. 10 b), that will likely become the next landward position for the grounding line. Subsequently, another cavity on a retrograde slope may cause a rapid retreat of the grounding line down to km 37.5, where the bed slope changes to a prograde slope, which should slow down the grounding line's recession.

While tides allow for the renewal of the water inside the cavities around the pinning points, the glacier uplift caused by tides and atmospheric pressure also allows periodic seawater intrusions everywhere within the ~~GZ~~grounding zone. On Petermann Glacier, 400 km southeast of Milne Fiord, Ciraci et al. (2023) estimated that submarine melt rates were up to 80 m/yr in the ~~GZ~~ grounding zone due to seawater intrusions. Sea-water intrusion is also thought to be an important component of the recent retreat of Thwaites Glacier (Rignot et al. 2024) and Jakobshavn Isbræ (Kim eat al. 2024). At Milne Fiord, where ~~SSH~~ tidal range is about 0.41 m, a 2.4 km and a 1 km incursion along and across the eastern part of the fjord, respectively, corresponds to approximately 11.4 m^3/s of seawater moving in (during flood tide) or out (during ebb tide) of the Milne Glacier ~~GZ~~grounding zone. Given that this water is roughly 1°C above the local freezing point at 150 m depth (Hamilton 2021; Bonneau et al., 2024b), these intrusions have the potential to melt ice at a rate of~~about~~ 0.15 m^3/s ~~of ice~~. This is comparable to the estimated submarine melt rate along the entire ~5 km-wide submerged glacier front, which is 0.82 m^3/s (Bonneau et al., 2024a), underscoring the potential effect of seawater intrusions in Milne Glacier ~~GZ~~ grounding-line retreat.

The grounding zone plays a crucial role in glacier dynamics, as it controls the discharge of ice from the grounded portion of the glacier (Schoof, 2007). The computed average annual velocity along the transects varied from 145 to 166 m yr^{-1} in the grounding zone during the study period, which was close to results (i.e., between 160 and 190 m yr^{-1}) for 1990s reported by Millan et al., (2017) but higher than observed velocities over recent years. The velocity increase observed in the 1990s was followed by the development of the western notch between 1992 and 2011 (Antropova et al., 2024). More recently, between

Formatted: Not Highlight

Formatted: Not Highlight

Formatted: Superscript

2010 and 2020, the glacier velocity in the flexure zone ranged from 80 to 160 m yr^{-1} with peak values occurring between 2018 and 2020 (Wychen et al., 2020). This study documents further glacier acceleration in the grounding zone, accompanied by the formation of the eastern notch, which was preceded by grounding-line retreat (Antropova et al., 2024). These findings support the idea that Milne Glacier, currently resting on a retrograde slope in its grounding zone, is likely susceptible to marine ice-sheet instability. The newly observed notch in the eastern part of the glacier might suggest future changes in the glacier dynamics.

Our ~~D~~DInSAR observations of Milne Glacier reveals that its grounding~~-~~line retreat along the western and eastern transects were driven by the sea water intrusion upstream of the pinning point, which can lead to a 10%–50% increase in the volume loss from marine-terminating glaciers and ice sheets (Robel et al., 2022). The dramatic Milne Glacier grounding~~-~~line ~~1992-2023~~ retreat between 1992 and 2023 along its western margin started with a notch, which was associated with a pinning point and seawater intrusion behind it (2011 ~~D~~DInSAR ~~results~~ image in Fig. 5 by Antropova et al., 2024). This notch widened towards the glacier centre between 2011 and 2023. The present study shows that the eastern margin has recently also been experiencing an extensive ungrounding around a pinning point, with a new notch likely expanding towards the glacier centre. Thus, the SAR-derived patterns of the grounding~~-~~line retreat suggest that ice ungrounding progresses from pinning points towards the glacier centre driving ice deterioration and further grounding~~-~~line retreat. Comprehensive in~~-~~situ observations of ice thinning and melt processes near pinning points combined with detailed bed information and frequent satellite ~~D~~DInSAR observations would provide additional details and insights about processes causing ice deterioration near the pinning points.

Conclusions

Our study demonstrated the benefits of the RCM 4-day high-resolution coherent change detection acquisition cycle for monitoring of glacier ~~FZs~~ flexure-zones and grounding~~-~~line migration at a high temporal resolution from four different orbits. These relatively frequent RCM data acquisitions spanning from February 2023 to September 2024 allowed us to examine a large SAR dataset to better understand the Milne Glacier flexure-zone~~FZ~~ intra-annual migration pattern, while also taking into account the SAR viewing geometry and quantifying uncertainties associated with glacier velocity variability and ice bending. In addition, we were able to support our ~~D~~DInSAR observations with in~~-~~situ glacier-specific and environmental datasets ~~and explore the presence of a seasonal component related to glacier stable and unstable velocities in our observations~~. The most reliable DInSAR results, with low LOShV and LOShB errors and associated uncertainties within one pixel, were obtained from orbits with low incidence angles and ascending tracks. Our results showed that Milne Glacier ~~FZ~~ flexure-zone intra-annual migration is driven by tidal cycles and atmospheric pressure~~, the latter of which can play an important role for fiords with small tidal ranges~~. ~~DDInSAR results were reliable despite velocity variations during the unstable season, but the effect of viewing geometry requires further investigations.~~ Bed geometry, specifically pinning points, plays a crucial role in shaping the

~~FZ~~ flexure zone and governing grounding~~-~~line retreat. In ~~-~~situ observations of melt processes near pinning points could provide further insight into their influence on grounding~~-~~line dynamics.

Continuous frequent satellite-based monitoring of changes in the ~~FZ~~ flexure zone ~~and GZ~~ of marine-terminating glaciers, as demonstrated in the present study using RCM SAR~~such as our work here with RCM SAR~~, serves as an efficient tool to explore short-term migration of these crucial zones. Consistent and frequent SAR observations over Arctic and Antarctic glaciers in combination with improved datasets on their bed geometry and ice thinning will ultimately improve our understanding of ice deterioration in the ~~GZ~~ grounding zone that, in turn, will improve our glacier modeling capabilities.

Appendix A

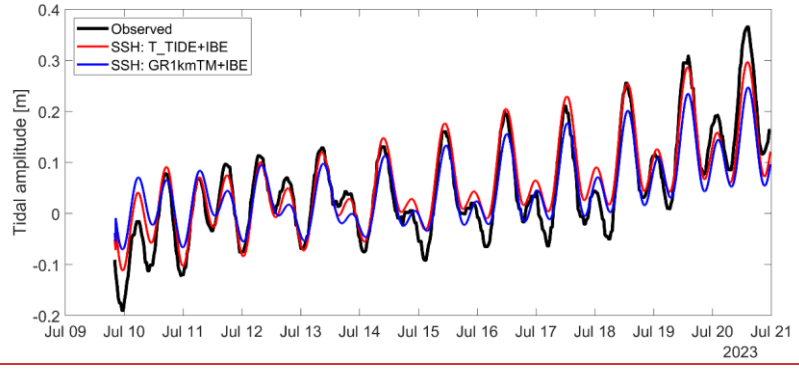


Figure A1: Observed tides measured in situ with a moored pressure sensor in July 2023 (black) and computed sea surface heights (SSH) using IBE-corrected T_TIDE simulations (red) and the Gr1kmTM model (blue) (Howard and Padman, 2021). IBE was calculated based on GEM model pressure records. The correlation between the observed and computed SSH is 0.96 for T_TIDE and 0.93 for Gr1kmTM, with RMSE values of 3.4 cm and 4.6 cm, respectively.

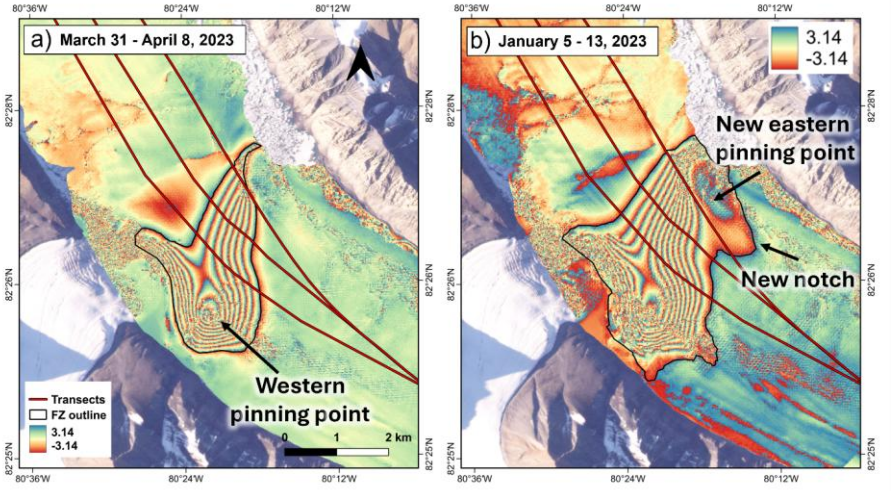


Figure A2: DInSAR image examples from orbit 103 showing: a) the flexure zone without the eastern notch, b) the flexure zone with the newly formed notch around the eastern pinning point.

Formatted: Highlight

Formatted: Centered

Formatted: Caption, Centered, Space Before: 0 pt, After: 0 pt

Formatted: Font: 9 pt, English (United Kingdom), Pattern: Clear (White)

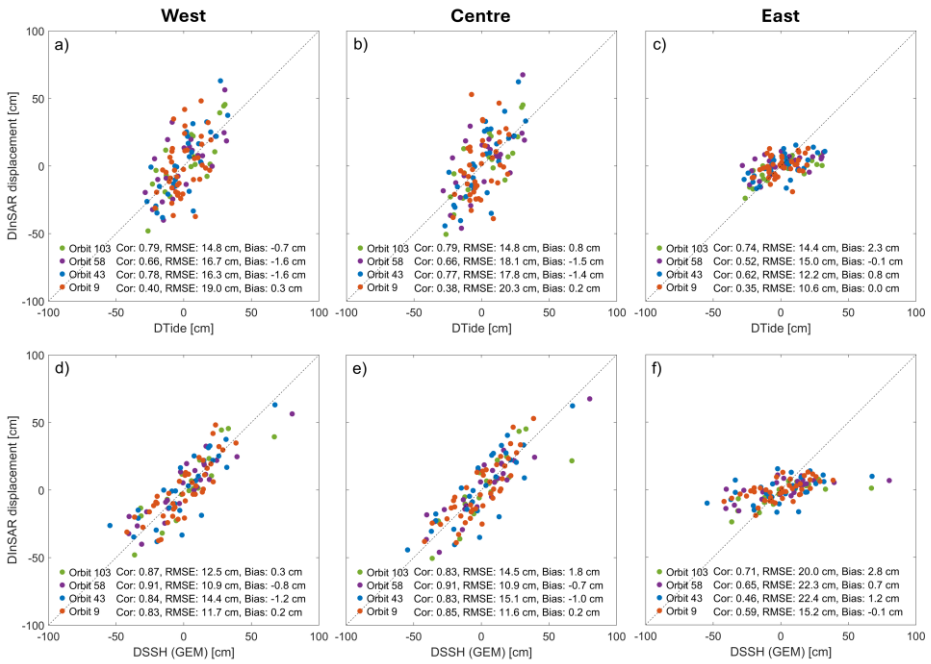


Figure A3: Relationship results for the three transects. Upper panels: relationships between DInSAR displacement and displacement of simulated tides (DTide) without IBE for the: a) western, b) central, and c) eastern transects. Lower panels: relationships between DInSAR displacement and displacement of sea surface height (DSSH) based on Global Environmental Multiscale (GEM) model for the: d) western, e) central, and f) eastern transects. The different orbits are denoted by coloured symbols. 'Cor' - the Pearson correlation coefficient, 'RMSE' - Root mean square error, the 1:1 is plotted as a dashed line.

Formatted: Centered

Formatted: Centered

Formatted: Normal, Left

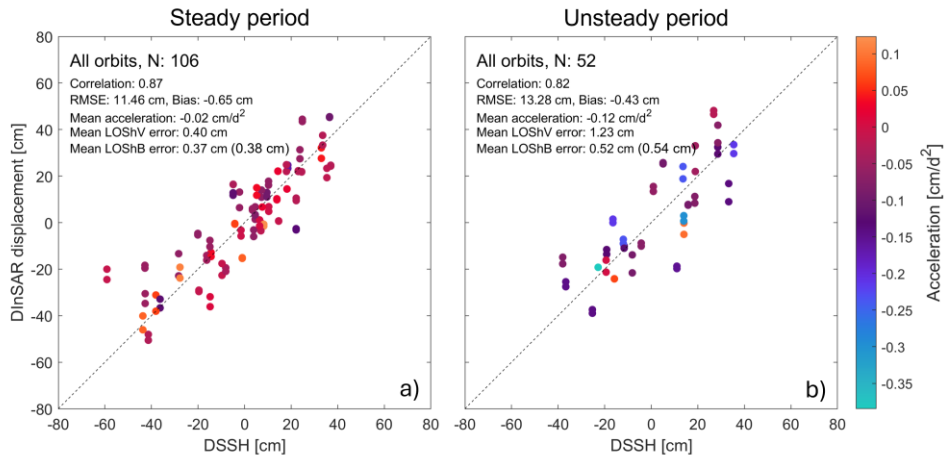


Figure A4: DInSAR-derived displacements versus DSSH combined along the western and central transects with respect to the two glacier velocity periods. a) Steady period with minimal changes in velocities and b) Unsteady period with more pronounced changes in velocities as defined in Fig. 2. LOShV represents error due to variable velocity based on in situ GNSS records, and LOShB represents error due to ice surface extension or compression from tidal bending along the central (western) transect.

Formatted: Centered

Formatted: Caption, Centered

Appendix B

We assume that the glacier vertical displacement can be described by the ~~single~~multi-frequency harmonic function given by Eq. 1. Determining all the coefficients at once represents an ill-posed problem that requires regularization, but the resulting solution was still found to be unstable exhibiting high-frequency fluctuations. To achieve a more stable solution, instead to deriving all the coefficients at once, we chose to derive the coefficients sequentially starting with the frequency corresponding to the most dominant tidal constituent (j=1) and finishing with the frequency corresponding to the least dominant tidal constituent (j=N).

First, we determined the coefficients corresponding to the dominant semidiurnal M2 tidal constituent (j=1). ~~Then, e~~Each observed SAR-derived double difference displacement, Δd_i (i is the number of observations: 1, 2, … n) is given by the following linear combination with unknown coefficients a_j, b_j, and c_j: ~~a_k (k = 1,2,3).~~

$$\Delta d_i = a_{\sout{1}j} S_i + b_{\sout{j2}} C_i + c_{\sout{j3}} H_i, \quad \text{(BA1)}$$

where

$$S_i = [\sin(\omega_j t_2^{(i)}) - \sin(\omega_j t_1^{(i)})] - [\sin(\omega_j t_4^{(i)}) - \sin(\omega_j t_3^{(i)})], \quad \text{(B2)}$$

$$C_i = [\cos(\omega_j t_2^{(i)}) - \cos(\omega_j t_1^{(i)})] - [\cos(\omega_j t_4^{(i)}) - \cos(\omega_j t_3^{(i)})], \quad \text{(B3)}$$

$$H_i = [H(t_2^{(i)}) - H(t_1^{(i)})] - [H(t_4^{(i)}) - H(t_3^{(i)})], \quad \text{(B4)}$$

~~$S_i = [\sin(\omega t_2^{(i)}) - \sin(\omega t_1^{(i)})] - [\sin(\omega t_4^{(i)}) - \sin(\omega t_3^{(i)})],$~~ ~~(A2)~~

~~$C_i = [\cos(\omega t_2^{(i)}) - \cos(\omega t_1^{(i)})] - [\cos(\omega t_4^{(i)}) - \cos(\omega t_3^{(i)})],$~~ ~~(A3)~~

~~$H_i = [H(t_2^{(i)}) - H(t_1^{(i)})] - [H(t_4^{(i)}) - H(t_3^{(i)})],$~~ ~~(A4)~~

where $t_j^{(i)}$ are known times of RCM SAR data acquisitions represented as serial date numbers (e.g., the MATLAB notation of 'datenum') and ω is the circular frequency corresponding to the dominant semi diurnal M2 tidal constituent.

For the set of n ~~D~~DInSAR observations, the following system of linear equations can be obtained:

$$MA = D, \quad \text{(BA5)}$$

where:

$$M = \begin{bmatrix} S_1 & C_1 & H_1 \\ S_2 & C_2 & H_2 \\ \cdots & \cdots & \cdots \\ S_n & C_n & H_n \end{bmatrix}, D = \begin{bmatrix} \Delta d_1 \\ \Delta d_2 \\ \cdots \\ \Delta d_n \end{bmatrix}, A = \begin{bmatrix} a_j \\ b_j \\ c_j \end{bmatrix} \cdot \sout{\begin{bmatrix} a_1 \\ a_2 \\ a_3 \end{bmatrix}}. \quad \text{(BA6)}$$

Then, the unknown coefficients A can be derived using Tikhonov's regularization approach as follows:

$$A = (M^T M + \lambda^2 I)^{-1} M^T D, \quad \text{(B7)}$$

where I is the identity 3×3 matrix, and λ is the regularization parameter. We note that for the dominant frequency ($j = 1$) the least-square problem is well-posed, so the regularization is not required (i.e., $\lambda = 0$), but for the other frequencies ($j > 1$) regularization must be applied, and λ was chosen to be 10.

Once A is found for the first frequency ($j = 1$), D can be updated as $D \leftarrow D - MA$, and the process from (A1) to (A7) is repeated. By running the same approach for the other frequencies $j = 2..N$, all the coefficients a_j and b_j can be determined. The final solution for coefficient $c = \sum_{j=1}^{N} c_j$.

~~Then, the unknown coefficients are derived using the least squares method as follows:~~

~~$A = (M^T M)^{-1} M^T D.$ (A7)~~

Data availability: The authors do not have permission to share raw RCM data, but it can be accessed by- registering a vetted user account (https://www.asc-csa.gc.ca/eng/satellites/radarsat/access-to-data/about.asp). InSAR results, as well as other field, simulated, and modeled data used in this study, are available upon request. Tthe IceBridge airborne radar data (IceBridge MCoRDS L2 Ice Thickness, Version 1 [IRMCR2_20140401_03], https://doi.org/10.5067/GDQ0CUCVTE2Q) are freely available at https://nsidc.org/data/irmcr2/versions/1., ~~other field and modeled data can be shared by request.~~

Author contribution: YA: collected field data, developed methodology and algorithms to conduct the data processing and analysis, participated in the funding acquisition, prepared the initial manuscript; DM: supervised the research project, acquired funding, managed field work, collected data; SS: developed software and conducted SAR data processing; AK: tasked RCM satellites, participated in the data analysis; JB: collected and processed field data. All: conceptualized the research project, reviewed, and edited the manuscript.

Competing interests: The authors declare that they have no conflict of interest.

Acknowledgements: We are thankful to the Polar Continental Shelf Program for the logistical support that greatly facilitated all field work activities related to this study, and to the Research Computing Services at Carleton University for IT support. We thank all members of the 2014, 2016, 2019, 2022, and 2023 field campaigns in Milne Fiord. We are grateful to Adam Garbo for building the GNSS instruments. We thank the Canadian Space Agency for providing the RADARSAT Constellation Mission (RCM) imagery. The airborne radar data used in this study were acquired by NASA's Operation IceBridge (Paden et al., 2019; https://doi.org/10.5067/GDQ0CUCVTE2Q). We acknowledge the use of data products from CReSIS generated with support from the University of Kansas, NSF grant ANT- 0424589, and NASA Operation IceBridge grant NNX16AH54G. We thank Ian Delaney for editorial handling, and Sam Herreid and Christian T. Wild for reviewing our manuscript and providing valuable and insightful feedback.

Financial support: This project was supported by the: Natural Sciences and Engineering Research Council of Canada (YA: CGS M 2019, and PGSD3–546559-2020; DM: Discovery Grant and Northern Research Supplement RGPIN-2016-06244, RGPNS-2022-04875), W. Garfield Weston Foundation (YA: 2019–2020 Northern Research and Extended Stay Awards), Canada Foundation for Innovation (DM:31410), Ontario Research Foundation (DM: 31410), Polar Continental Shelf Program (DM: 627–18; 651-14, 636-16, 651–19, 665-22, 655–23), ArcticNet (a Network of Centres of Excellence of Canada) GO-Ice project (YA,DM, and JB), Polar Knowledge Canada (YA and JB: Northern Scientific Training Program 2019, 2022, and 2023).

References

Antropova, Y. K., Mueller, D., Samsonov, S. V., Komarov, A. S., Bonneau, J., and Crawford, A. J.: Grounding-line retreat of Milne Glacier, Ellesmere Island, Canada over 1966–2023 from satellite, airborne, and ground radar data, *Remote Sens. Environ.*, **315**, 114478, https://doi.org/10.1016/j.rse.2024.114478, 2024.

Black, T. E. and Joughin, I.: Multi-decadal retreat of marine-terminating outlet glaciers in northwest and central-west Greenland, *The Cryosphere*, **16**, 807–824, https://doi.org/10.5194/tc-16-807-2022, 2022.

Bonneau, J., Laval, B. E., Mueller, D., Hamilton, A. K., and Crawford, A. J.: Heat fluxes in a glacial fjord: the role of buoyancy-driven circulation and offshore forcing, *Geophys. Res. Lett.*, https://doi.org/10.1029/2024GL111242, 2024a.

Bonneau, J., Laval, B. E., Mueller, D., Hamilton, A. K., and Forrest, A. L.: Unsteady circulation in a glacial fjord: a multiyear modeling study of Milne Fiord, *J. Geophys. Res. Oceans*, **129**, e2023JC020140, https://doi.org/10.1029/2023JC020140, 2024b.

Buehner, M., McTaggart-Cowan, R., Beaulne, A., Charette, C., Garand, L., Heilliette, S., Lapalme, E., Laroche, S., Macpherson, S. R., Morneau, J., and Zadra, A.: Implementation of deterministic weather forecasting systems based on ensemble–variational data assimilation at Environment Canada. Part I: The global system, *Mon. Weather Rev.*, https://doi.org/10.1175/MWR-D-14-00354.1, 2015.

Carnahan, E., Catania, G., and Bartholomaus, T. C.: Observed mechanism for sustained glacier retreat and acceleration in response to ocean warming around Greenland, *The Cryosphere*, **16**, 4305–4317, https://doi.org/10.5194/tc-16-4305-2022, 2022.

Chartrand, A. M., Howat, I. M., Joughin, I. R., and Smith, B. E.: Thwaites Glacier thins and retreats fastest where ice-shelf channels intersect its grounding zone, *The Cryosphere*, **18**, 4971–4992, https://doi.org/10.5194/tc-18-4971-2024, 2024.

Chen, H., Rignot, E., Scheuchl, B., and Ehrenfeucht, S.: Grounding zone of Amery Ice Shelf, Antarctica, from differential synthetic-aperture radar interferometry, *Geophys. Res. Lett.*, **50**, e2022GL102430, https://doi.org/10.1029/2022GL102430, 2023.

Ciracì, E., Rignot, E., Scheuchl, B., Tolpekin, V., Wollersheim, M., An, L., Milillo, P., Bueso-Bello, J.-L., Rizzoli, P., and Dini, L.: Melt rates in the kilometer-size grounding zone of Petermann Glacier, Greenland, before and during a retreat, *Proc. Natl. Acad. Sci. USA*, **120**, e2220924120, https://doi.org/10.1073/pnas.2220924120, 2023.

CReSIS: 2014 Greenland P3 data, digital media, Lawrence, Kansas, USA, available at: http://data.cresis.ku.edu/, 2021.

Costantini, M.: A novel phase unwrapping method based on network programming, *IEEE Trans. Geosci. Remote Sens.*, **36**, 813–821, https://doi.org/10.1109/36.673674, 1998.

Formatted: Space After: 6 pt

Formatted: English (Canada)

Formatted: English (Canada)

Formatted: English (Canada)

Field Code Changed

Freer, B. I. D., Marsh, O. J., Hogg, A. E., Fricker, H. A., and Padman, L.: Modes of Antarctic tidal grounding line migration revealed by ICESat-2 laser altimetry, *The Cryosphere*, **17**, 4079–4101, https://doi.org/10.5194/tc-17-4079-2023, 2023.

Fricker, H. A., Coleman, R., Padman, L., Scambos, T. A., Bohlander, J., and Brunt, K. M.: Mapping the grounding zone of the Amery Ice Shelf, East Antarctica using InSAR, MODIS and ICESat, *Antarct. Sci.*, **21**, 515–532, https://doi.org/10.1017/S0954102009990023X, 2009.

Garbo, A.: Cryologger glacier velocity tracker (v2.3.1) [software], available at: https://github.com/cryologger/glacier-velocity-tracker, 2024.

Hamilton, A. K., Mueller, D., and Laval, B. E.: Ocean modification and seasonality in a northern Ellesmere Island glacial fjord prior to ice shelf breakup: Milne Fiord, *J. Geophys. Res. Oceans*, **126**, e2020JC016975, https://doi.org/10.1029/2020JC016975, 2021.

Holmes, F. A., Barnett, J., Åkesson, H., Morlighem, M., Nilsson, J., Kirchner, N., and Jakobsson, M.: Sea level rise contribution from Ryder Glacier in northern Greenland varies by an order of magnitude by 2300 depending on future emissions, *The Cryosphere*, **19**, 2695–2714, https://doi.org/10.5194/tc-19-2695-2025, 2025.

Howard, S. L. and Padman, L.: Gr1kmTM: Greenland 1 kilometer tide model, Arctic Data Center, https://doi.org/10.18739/A2251FM3S, 2021.

Hu, J., Li, Z. W., Ding, X. L., Zhu, J. J., Zhang, L., and Sun, Q.: Resolving three-dimensional surface displacements from InSAR measurements: a review, *Earth-Sci. Rev.*, **133**, 1–17, https://doi.org/10.1016/j.earscirev.2014.02.005, 2014.

Jeffries, M. O.: Milne Glacier, northern Ellesmere Island, NWT, Canada: a surging glacier?, *J. Glaciol.*, **30**, 251–253, 1984.

Kochtitzky, W. and Copland, L.: Retreat of Northern Hemisphere marine-terminating glaciers, 2000–2020, *Geophys. Res. Lett.*, **49**, e2021GL096501, https://doi.org/10.1029/2021GL096501, 2022.

Kim, J. H., Rignot, E., Holland, D., and Holland, D. M.: Seawater intrusion at the grounding line of Jakobshavn Isbræ, Greenland, from terrestrial radar interferometry, *Geophys. Res. Lett.*, **51**, e2023GL106181, https://doi.org/10.1029/2023GL106181, 2024.

MDA Space: RADARSAT Constellation Mission product specification, available at: https://download-telecharger.services.geo.ca/..., 2021.

Millan, R., Jager, E., Mouginot, J., Wood, M. H., Larsen, S. H., Mathiot, P., Jourdain, N. C., and Bjørk, A.: Rapid disintegration and weakening of ice shelves in North Greenland, *Nat. Commun.*, **14**, 6914, https://doi.org/10.1038/s41467-023-42198-2, 2023.

Millan, R., Mouginot, J., and Rignot, E.: Mass budget of the glaciers and ice caps of the Queen Elizabeth Islands, Canada, from 1991 to 2015, *Environ. Res. Lett.*, **12**, 024016, https://doi.org/10.1088/1748-9326/aa5b04, 2017.

Milillo, P., Rignot, E., Mouginot, J., Scheuchl, B., Morlighem, M., Li, X., and Salzer, J. T.: Short-term grounding zone dynamics of Pine Island Glacier, *Geophys. Res. Lett.*, **44**, 10436–10444, https://doi.org/10.1002/2017GL074320, 2017.

Milillo, P., Rignot, E., Rizzoli, P., Scheuchl, B., Mouginot, J., Bueso-Bello, J. L., Prats-Iraola, P., and Dini, L.: Rapid glacier retreat rates observed in West Antarctica, *Nat. Geosci.*, **15**, 51–56, https://doi.org/10.1038/s41561-021-00877-z, 2022.

Mohajerani, Y., Jeong, S., Scheuchl, B., Velicogna, I., Rignot, E., and Milillo, P.: Automatic delineation of glacier grounding lines using deep learning, *Sci. Rep.*, **11**, 1–13, https://doi.org/10.1038/s41598-021-84309-3, 2021.

Morlighem, M., Wood, M., Seroussi, H., Choi, Y., and Rignot, E.: Modeling the response of northwest Greenland to enhanced ocean thermal forcing, *The Cryosphere*, **13**, 723–734, https://doi.org/10.5194/tc-13-723-2019, 2019.

Mortimer, C. A., Copland, L., and Mueller, D. R.: Volume and area changes of the Milne Ice Shelf, Ellesmere Island, Nunavut, Canada, since 1950, *J. Geophys. Res. Earth Surf.*, **117**, https://doi.org/10.1029/2011JF002074, 2012.

Mueller, D., Copland, L., and Jeffries, M. O.: Changes in Canadian Arctic ice shelf extent since 1906, in: *Arctic Ice Shelves and Ice Islands*, 109–148, https://doi.org/10.1007/978-94-024-1101-0_5, 2017.

Natural Resources Canada (NRCan): Canadian Spatial Reference System precise point positioning (CSRS-PPP) service, available at: https://webapp.csrs-scrs.nrcan-rncan.gc.ca/geod/tools-outils/ppp.php, 2024.

Paden, J., Li, J., Leuschen, C., Rodriguez-Morales, F., and Hale, R.: IceBridge MCoRDS L2 ice thickness, Version 1, NASA National Snow and Ice Data Center Distributed Active Archive Center, https://doi.org/10.5067/GDQ0CUCVTE2Q, 2019.

Padman, L., King, M., Goring, D., Corr, H., and Coleman, R.: Ice-shelf elevation changes due to atmospheric pressure variations, *J. Glaciol.*, **49**, 521–526, https://doi.org/10.3189/172756503781830386, 2003.

Pawlowicz, R., Beardsley, B., and Lentz, S.: Classical tidal harmonic analysis including error estimates in MATLAB using T_TIDE, *Comput. Geosci.*, **28**, 929–937, https://doi.org/10.1016/S0098-3004(02)00013-4, 2002.

Planet Team: Planet application program interface: in space for life on Earth, San Francisco, CA, available at: https://api.planet.com/, 2024.

Poinelli, M., Nakayama, Y., Larour, E., Vizcaino, M., and Riva, R.: Ice-front retreat controls on ocean dynamics under Larsen C Ice Shelf, Antarctica, *Geophys. Res. Lett.*, **50**, e2023GL104588, https://doi.org/10.1029/2023GL104588, 2023.

Porter, C., et al.: ArcticDEM, Version 4.1, Harvard Dataverse, https://doi.org/10.7910/DVN/3VDC4W, 2023.

Rantanen, M., Karpechko, A. Y., Lipponen, A., Nordling, K., Hyvärinen, O., Ruosteenoja, K., Vihma, T., and Laaksonen, A.: The Arctic has warmed nearly four times faster than the globe since 1979, *Commun. Earth Environ.*, **3**, 168, https://doi.org/10.1038/s43247-022-00498-3, 2022.

Rignot, E., Ciracì, E., Scheuchl, B., Tolpekin, V., Wollersheim, M., and Dow, C.: Widespread seawater intrusions beneath the grounded ice of Thwaites Glacier, West Antarctica, *Proc. Natl. Acad. Sci. USA*, **121**, e2404766121, https://doi.org/10.1073/pnas.2404766121, 2024.

Rignot, E.: Tidal motion, ice velocity and melt rate of Petermann Gletscher, Greenland, measured from radar interferometry, *J. Glaciol.*, **42**, 476–485, https://doi.org/10.3189/S0022143000003464, 1996.

Robel, A. A., Wilson, E., and Seroussi, H.: Layered seawater intrusion and melt under grounded ice, *The Cryosphere*, **16**, 451–469, https://doi.org/10.5194/tc-16-451-2022, 2022.

Rocca, F., Prati, C., and Ferretti, A.: Space-borne SARs: impact of wavelengths and scan modes on ground motion studies, *Ann. GIS*, **16**, 69–79, https://doi.org/10.1080/19475683.2010.492124, 2010.

Samsonov, S.: Multidimensional small baseline subset (MSBAS) software for constrained and unconstrained deformation analysis, *Can. J. Remote Sens.*, **50**, 2424753, https://doi.org/10.1080/07038992.2024.2424753, 2024.

Samsonov, S., Tiampo, K., and Cassotto, R.: Measuring the state and temporal evolution of glaciers in Alaska and Yukon using SAR-derived 3D time series, *The Cryosphere*, **15**, 4221–4239, https://doi.org/10.5194/tc-15-4221-2021, 2021.

Schoof, C.: Ice sheet grounding line dynamics: steady states, stability, and hysteresis, *J. Geophys. Res. Earth Surf.*, **112**, https://doi.org/10.1029/2006JF000664, 2007.

Tsai, V. C. and Gudmundsson, G. H.: An improved model for tidally modulated grounding-line migration, *J. Glaciol.*, **61**, 216–222, https://doi.org/10.3189/2015JoG14J152, 2015.

Van Wychen, W. V., Burgess, D., Kochtitzky, W., Nikolic, N., Copland, L., and Gray, L.: RADARSAT-2-derived glacier velocities and dynamic discharge estimates for the Canadian High Arctic, *Can. J. Remote Sens.*, **46**, 695–714, https://doi.org/10.1080/07038992.2020.1859359, 2020.

Veillette, J., Mueller, D. R., Antoniades, D., and Vincent, W. F.: Arctic epishelf lakes as sentinel ecosystems: past, present and future, *J. Geophys. Res. Biogeosci.*, **113**, 2008.

Werner, C., Wegmüller, U., Strozzi, T., and Wiesmann, A.: GAMMA SAR and interferometric processing software, in: *ERS–ENVISAT Symposium*, Gothenburg, Sweden, 16–20, 2000.

Wild, C. T., Drews, R., Neckel, N., Lee, J., Kim, S., Han, H., Lee, W. S., Helm, V., Rosier, S. H. R., Marsh, O. J., and Rack, W.: Monitoring shear-zone weakening in East Antarctic outlet glaciers through differential InSAR measurements, *The Cryosphere*, **19**, 4533–4554, https://doi.org/10.5194/tc-19-4533-2025, 2025.

Wild, C. T., Marsh, O. J., and Rack, W.: Unraveling InSAR-observed Antarctic ice-shelf flexure using 2-D elastic and viscoelastic modeling, *Front. Earth Sci.*, **6**, https://doi.org/10.3389/feart.2018.00028, 2018.

Wild, C. T., Marsh, O. J., and Rack, W.: Viscosity and elasticity: a model intercomparison of ice-shelf bending in an Antarctic grounding zone, *J. Glaciol.*, **63**, 573–580, https://doi.org/10.1017/jog.2017.15, 2017.

Wunsch, C. and Stammer, D.: Atmospheric loading and the oceanic "inverted barometer" effect, *Rev. Geophys.*, **35**, 79–107, https://doi.org/10.1029/96RG03037, 1997.

Antropova, Y. K., Mueller, D., Samsonov, S. V., Komarov, A. S., Bonneau, J., & Crawford, A. J. (2024). Grounding line retreat of Milne Glacier, Ellesmere Island, Canada over 1966–2023 from satellite, airborne, and ground radar data. *Remote Sensing of Environment*, *315*, 114478. https://doi.org/10.1016/j.rse.2024.114478

Bonneau, J., Laval, B.E., Mueller, D., Hamilton, A.K., Antropova, Y.K., 2024a. Heat Fluxes in a Glacial Fjord: The Role of Buoyancy-Driven Circulation and Offshore Forcing. Geophys. Res. Lett. https://doi.org/10.1029/2024GL111242.

Bonneau, J., Laval, B.E., Mueller, D., Hamilton, A.K., Forrest, A.L., 2024b. Unsteady circulation in a Glacial Fjord: a multiyear modeling study of Milne fiord. J. Geophys. Res. Oceans 129 (6), e2023JC020140. https://doi.org/10.1029/2023JC020140.

Buehner, M., McTaggart-Cowan, R., Beaulne, A., Charette, C., Garand, L., Heilliette, S., Lapalme, E., Laroche, S., Macpherson, S. R., Morneau, J., & Zadra, A. (2015). Implementation of Deterministic Weather Forecasting Systems Based on Ensemble–Variational Data Assimilation at Environment Canada. Part I: The Global System.

Chen, C. W., & Zebker, H. A. (2002). Phase unwrapping for large SAR interferograms: Statistical segmentation and generalized network models. *IEEE Transactions on Geoscience and Remote Sensing*, *40*(8), 1709–1719. IEEE Transactions on Geoscience and Remote Sensing. https://doi.org/10.1109/TGRS.2002.802453

Ciracì, E., Rignot, E., Scheuchl, B., Tolpekin, V., Wollersheim, M., An, L., Milillo, P., Bueso-Bello, J.-L., Rizzoli, P., & Dini, L. (2023). Melt rates in the kilometer-size grounding zone of Petermann Glacier, Greenland, before and during a retreat. *Proceedings of the National Academy of Sciences*, *120*(20), e2220924120. https://doi.org/10.1073/pnas.2220924120

CReSIS. 2021. In: 2014 Greenland P3 Data, Lawrence, Kansas. Digital Media, USA.

Freer, B. I. D., Marsh, O. J., Hogg, A. E., Fricker, H. A., & Padman, L. (2023). Modes of Antarctic tidal grounding line migration revealed by Ice, Cloud, and land Elevation Satellite-2 (ICESat-2) laser altimetry. The Cryosphere, 17(9), 4079–4101. https://doi.org/10.5194/tc-17-4079-2023

Fricker, H. A., Coleman, R., Padman, L., Scambos, T. A., Bohlander, J., & Brunt, K. M. (2009). Mapping the grounding zone of the Amery Ice Shelf, East Antarctica using InSAR, MODIS and ICESat. Antarctic Science, 21(5), 515–532. https://doi.org/10.1017/S0954102009990023X

Garbo, A. (2024). Cryologger Glacier Velocity Tracker (Version 2.3.1) [Computer software]. https://github.com/cryologger/glacier-velocity-tracker

Hamilton, A. K., Mueller, D., & Laval, B. E. (2021). Ocean Modification and Seasonality in a Northern Ellesmere Island Glacial Fjord Prior to Ice Shelf Breakup: Milne Fiord. Journal of Geophysical Research: Oceans, 126(7), e2020JC016975. https://doi.org/10.1029/2020JC016975

Formatted: English (Canada)

Intergovernmental Panel on Climate Change (IPCC). Climate Change 2021 – The Physical Science Basis: Working Group I Contribution to the Sixth Assessment Report of the Intergovernmental Panel on Climate Change. Cambridge University Press; 2023.

Jeffries, M. O. (2002), Ellesmere Island ice shelves and ice islands, in Satellite Image Atlas of Glaciers of the World: North America, edited by R. S. Williams Jr. and J. G. Ferrigno, pp. J147–J164, U.S. Geol. Surv., Washington, D. C.

Jeffries, M. O. (1985), Physical, chemical and isotopic investigations of Ward Hunt Ice Shelf and Milne Ice Shelf, Ellesmere Island, NWT, PhD thesis, Dep. of Geogr., Univ. of Calgary, Alberta, Canada.

Jeffries, M.O., 1984. Milne glacier, northern Ellesmere Island, N.W.T., Canada: a surging glacier? J. Glaciol. 30 (105), 251–253

Kochtitzky, W., & Copland, L. (2022). Retreat of Northern Hemisphere Marine-Terminating Glaciers, 2000–2020. *Geophysical Research Letters*, *49*(3), e2021GL096501. https://doi.org/10.1029/2021GL096501

Kim, J. H., Rignot, E., Holland, D., & Holland, D. (2024). Seawater Intrusion at the Grounding Line of Jakobshavn Isbræ, Greenland, From Terrestrial Radar Interferometry. Geophysical Research Letters, 51(6), e2023GL106181.

Millan, R., Jager, E., Mouginot, J., Wood, M. H., Larsen, S. H., Mathiot, P., Jourdain, N. C., & Bjørk, A. (2023). Rapid disintegration and weakening of ice shelves in North Greenland. *Nature Communications*, *14*(1), 6914. https://doi.org/10.1038/s41467-023-42198-2

Millan, R., Mouginot, J., & Rignot, E. (2017). Mass budget of the glaciers and ice caps of the Queen Elizabeth Islands, Canada, from 1991 to 2015. *Environmental Research Letters*, *12*(2), 024016. https://doi.org/10.1088/1748-9326/aa5b04

Milillo, P., Rignot, E., Rizzoli, P., Scheuchl, B., Mouginot, J., Bueso-Bello, J. L., Prats-Iraola, P., & Dini, L. (2022). Rapid glacier retreat rates observed in West Antarctica. *Nature Geoscience*, *15*(1), Article 1. https://doi.org/10.1038/s41561-021-00877-z

Milillo, P., Rignot, E., Rizzoli, P., Scheuchl, B., Mouginot, J., Bueso-Bello, J., & Prats-Iraola, P. (2019). Heterogeneous retreat and ice melt of Thwaites Glacier, West Antarctica. *Science Advances*, *5*(1), eaau3433. https://doi.org/10.1126/sciadv.aau3433

Mohajerani, Y., Jeong, S., Scheuchl, B., Velicogna, I., Rignot, E., & Milillo, P. (2021). Automatic delineation of glacier grounding lines in differential interferometric synthetic-aperture radar data using deep learning. *Scientific Reports*, *11*(1), Article 1. https://doi.org/10.1038/s41598-021-84309-3

Mortimer, C. A., Copland, L., & Mueller, D. R. (2012). Volume and area changes of the Milne Ice Shelf, Ellesmere Island, Nunavut, Canada, since 1950. Journal of Geophysical Research. Earth Surface; Washington, 117(4). http://dx.doi.org.proxy.library.carleton.ca/10.1029/2011JF002074

Mueller, D., Copland, L., Jeffries, M.O. (2017). Changes in Canadian Arctic ice shelf extent since 1906. In: Arctic Ice Shelves and Ice Islands, pp. 109–148. Doi: 10.1007/978-94-024-1101-0_5

Natural Resources Canada (NRCan). (2024). Canadian Spatial Reference System Precise Point Positioning (CSRS-PPP) service. Retrieved from https://webapp.csrs-scrs.nrcan-rncan.gc.ca/geod/tools-outils/ppp.php

Paden, J., Li, J., Leuschen, C., Rodriguez-Morales, F., Hale, R., 2010. Updated 2019. IceBridge MCoRDS L2 Ice Thickness, Version 1. [IRMCR2_20140401_03]. NASA National Snow and Ice Data Center Distributed Active Archive Center, Boulder, Colorado USA. .

Pawlowicz, R., Beardsley, B., Lentz, S., 2002. Classical tidal harmonic analysis including error estimates in MATLAB using T_TIDE. Comput. Geosci. 28 (8), 929–937. https://doi.org/10.1016/S0098-3004(02)00013-4.

Planet Team, 2017. Planet Application Program Interface. In Space for Life on Earth, San Francisco, CA. https://api.planet.com.

Poinelli, M., Nakayama, Y., Larour, E., Vizcaino, M., & Riva, R. (2023). Ice Front Retreat Controls on Ocean Dynamics Under Larsen C Ice Shelf, Antarctica. Geophysical Research Letters, 50(18), e2023GL104588. https://doi.org/10.1029/2023GL104588

Porter, Claire, et al., 2023, "ArcticDEM, Version 4.1", https://doi.org/10.7910/DVN/3VDC4W, Harvard Dataverse, V1.

Prager, B. T. (1983), Digital signal processing of UHF radio echo sounding data from Northern Ellesmere Island, MS thesis, Dep. of Geophys. and Astron., Univ. of British Columbia, Vancouver, Canada.

Rignot, E., Ciraci, E., Scheuchl, B., Tolpekin, V., Wollersheim, M., & Dow, C. (2024). Widespread seawater intrusions beneath the grounded ice of Thwaites Glacier, West Antarctica. *Proceedings of the National Academy of Sciences*, *121*(22), e2404766121. https://doi.org/10.1073/pnas.2404766121

Rignot, E. (1996). Tidal motion, ice velocity and melt rate of Petermann Gletscher, Greenland, measured from radar interferometry. Journal of Glaciology, 42(142), 476–485. https://doi.org/10.3189/S0022143000003464

Robel, A. A., Wilson, E., & Seroussi, H. (2022). Layered seawater intrusion and melt under grounded ice. The Cryosphere, 16(2), 451–469.

V. Samsonov, S. (2024). Multidimensional Small Baseline Subset (MSBAS) Software for Constrained and Unconstrained Deformation Analysis of Partially Coherent DInSAR and Speckle Offset Data. Canadian Journal of Remote Sensing, 50(1), 2424753. https://doi.org/10.1080/07038992.2024.2424753

Samsonov, S., Tiampo, K., & Cassotto, R. (2021). Measuring the state and temporal evolution of glaciers in Alaska and Yukon using synthetic aperture radar derived (SAR derived) 3D time series of glacier surface flow. *The Cryosphere*, *15*(9), 4221–4239. https://doi.org/10.5194/tc-15-4221-2021

Tsai, V. C., & Gudmundsson, G. H. (2015). An improved model for tidally modulated grounding line migration. *Journal of Glaciology*, *61*(226), 216–222. https://doi.org/10.3189/2015JoG14J152

Van Wychen, W. V., Burgess, D., Kochtitzky, W., Nikolic, N., Copland, L., & Gray, L. (2020). RADARSAT-2 Derived Glacier Velocities and Dynamic Discharge Estimates for the Canadian High Arctic: 2015–2020. *Canadian Journal of Remote Sensing*, *46*(6), 695–714. https://doi.org/10.1080/07038992.2020.1859359

Formatted: English (Canada)

Van Wychen, W., Davis, J., Burgess, D. O., Copland, L., Gray, L., Sharp, M., & Mortimer, C. (2016). Characterizing interannual variability of glacier dynamics and dynamic discharge (1999–2015) for the ice masses of Ellesmere and Axel Heiberg Islands, Nunavut, Canada. *Journal of Geophysical Research: Earth Surface*, *121*(1), 39–63. https://doi.org/10.1002/2015JF003708

Veillette, J., Mueller, D. R., Antoniades, D., & Vincent, W. F. (2008). Arctic epishelf lakes as sentinel ecosystems: Past, present and future. Journal of Geophysical Research: Biogeosciences, 113(G4).

Werner, C., Wegmüller, U., Strozzi, T., Wiesmann, A., 2000. GAMMA SAR and Interferometric Processing Software. ERS - ENVISAT Symposium, Gothenburg, Sweden, pp. 16–20

Wunsch, C., & Stammer, D. (1997). Atmospheric loading and the oceanic "inverted barometer" effect. *Reviews of Geophysics*, *35*(1), 79–107. https://doi.org/10.1029/96RG03037

Formatted: English (Canada)